
Wesleyan University

Exploring the Role of Environment in the Composition of ONC Proplyds

by

Jonas Powell
Class of 2019

A thesis submitted to the
faculty of Wesleyan University
in partial fulfillment of the requirements for the
Degree of Master of Arts

Middletown, Connecticut

April, 2018

*If people sat outside and looked at the stars each night,
I'll bet they'd live a lot differently.*

—CALVIN & HOBBES

Contents

| | | |
|----------|---|-----------|
| 1 | Introduction | 1 |
| 1.1 | Submillimeter Observations | 4 |
| 1.1.1 | Interferometry | 5 |
| 1.1.2 | Continuum Emission | 12 |
| 1.1.3 | Line Emission | 14 |
| 1.2 | Disk & The Role of Environment | 18 |
| 1.2.1 | The Minimum Mass (Extra-)Solar Nebula | 18 |
| 1.2.2 | Low- and High-Mass Star Forming Regions | 20 |
| 1.3 | d253-1536: A Misaligned Binary System | 24 |
| 1.3.1 | Local Environment & Features | 25 |
| 1.3.2 | Previous Observations | 26 |
| 1.4 | Summary of Contents | 28 |
| 2 | Observations | 29 |
| 3 | Results | 31 |
| 3.1 | Cloud Contamination | 31 |
| 3.2 | Line Data | 35 |
| 4 | Analysis | 39 |
| 4.1 | Gas Model | 39 |
| 4.1.1 | Establishing Physical Profiles | 40 |
| 4.1.2 | Generating a Model Image | 43 |
| 4.2 | Exploring Parameter Space | 44 |
| 4.2.1 | Grid Search | 45 |

| | | |
|---------------------|--------------------------------|-----------|
| 4.2.2 | Markov Chain Monte Carlo | 45 |
| 4.3 | Fitting Procedure | 48 |
| 4.3.1 | $\text{HCO}^+(4-3)$ Fit | 49 |
| 4.3.2 | $\text{HCN}(4-3)$ Fit | 51 |
| 4.3.3 | $\text{CO}(3-2)$ Fit | 52 |
| 5 | Discussion | 63 |
| 5.1 | Reflections on the Fits | 63 |
| 5.2 | Comparison with the Literature | 65 |
| 5.2.1 | Line Emission Modeling | 65 |
| 5.2.2 | Population Comparison | 68 |
| 5.3 | Remarks | 70 |
| 6 | Summary | 71 |
| Bibliography | | 73 |

List of Figures

- | | |
|---|---|
| 1.1 An edge-on slice of a protoplanetary disk is presented (Dullemond & Monnier 2010). As is visible in this graphic, significant radial segmentation of the disk exists, particularly between the inner gas disk and outer disk of gas, dust, and planetesimals. Also of note is the large vertical flaring that occurs at large radii. Since the observations that this thesis are based on were made with ALMA (discussed in §1.1.1), we are sensitive primarily to the outer reaches of the disk. | 3 |
| 1.2 Two example SEDs, accompanied by cartoon models to illustrate the various contributions of different elements of a disk and their influences on the SED (Hughes 2010). The dashed line corresponds to emission from the stellar photosphere, while the colored lines are blackbody curves corresponding to emission from regions of the disk with different temperatures. Since radio observations take place at longer (hundreds to thousands of microns) wavelengths, one may easily see that the stellar contribution in that regime is minimal. . | 6 |
| 12figure.caption.5 | |

| | |
|---|----|
| 1.5 Gas-to-dust ratios in protoplanetary disks in Lupus (?). The ratio is highly variable and rarely best described by the canonical value of 100:1. Blue points indicate detections, and gray triangles indicate upper limits. Error bars with downward arrows indicate sources detected in ^{13}CO but not C^{18}O , for which the authors did not establish lower mass limits. | 14 |
| 1.6 An example of a moment-one map of a protoplanetary disk, drawn from Rosenfeld et al. (2012). Colors correspond to intensity-weighted velocity; in other words, how quickly material is moving relative to the observer. One may consider this analogously to a spinning Frisbee, approaching the reader edge-on, where one half of the disk is spinning outwards (away from us) as the other side approaches. From this image, we immediately gain several pieces of information: for example, in this case, the disk as a whole is receding from view (since the velocity's "zero point", in yellow/green, is moving at 3 km/s), and that the disk's eastern half is spinning away from us, while the western half comes towards us. This gives us a quick understanding of the disk's kinematics. | 16 |
| 1.7 Proplyds in the Orion Nebula. The closer a proplyd is to a large, bright star, the more visibly windswept it is. Image courtesy of the Hubble Space Telescope Treasury Program on the Orion Nebula (Robberto et al. (2013)) | 21 |

| | | |
|------|--|----|
| 1.9 | <i>Left:</i> The masses of 70 ONC proplyds are plotted against their projected distance from the Orion Nebula's central O-star, θ^1 Ori C, drawn from surveys from ALMA and the SMA (Mann et al. 2014). Grey markers indicate 3σ upper limits for non-detections. The dashed line at $10 M_{Jup}$ indicates the minimum-mass solar nebula. As is clear from this plot, a statistically-significant correlation was found between disk mass and distance from θ^1 Ori C. <i>Right:</i> Radius is also affected by proximity to θ^1 Ori C (Eisner et al. 2018) | 25 |
| 1.11 | Images of V2434 Ori taken from Smith et al. (2005) on HST (Fig. 1.10a), Mann & Williams (2009) with the SMA at $880 \mu m$ (Fig. 1.10b), and Ricci et al. (2011) with the EVLA at 7mm (Fig. 1.10c). The ionization front is clearly visible in both the HST and EVLA observations, and the jet from disk A is visible in the HST image. | 26 |
| 1.13 | Moment-1 maps of $HCO^+(4-3)$, $HCN(4-3)$, $CO(3-2)$, and $CS(7-6)$ emission (left to right) in the present study's proplyds, observed with ALMA's Band 7. Each map shows intensity-weighted velocity, which allows us to trace the disks' kinematics. REWORK: considering making this a 2x2 grid, instead of 4 across. | 27 |
| 3.1 | HCO^+ Noise profiles | 34 |
| 3.2 | HCN Noise profiles | 34 |
| 3.3 | CO Noise profiles | 34 |
| 3.4 | CS Noise profiles | 34 |

| | | |
|-----|--|----|
| 3.5 | Zeroth moment map of CO emission, with and without a cut of all baseline's below $60 \text{ k}\lambda$ (left and right, respectively). Colors correspond to velocity-integrated intensity, while contours represent $\pm 3, 5, 7, \dots, 15\sigma$ transitions where 1σ is $0.257 \text{ Jy beam}^{-1} \text{ km s}^{-1}$. Negative contours are dashed. The beam is shown in the bottom left corner, with a diameter of $0.^{\circ}5$ which corresponds to 200 AU at 389 parsec. | 37 |
| 3.6 | First moment map of CO emission, with and without a cut of all baseline's below $60 \text{ k}\lambda$ (left and right, respectively). Colors correspond to intensity-weighted LSRK velocity, while contours represent $\pm 3, 5, 7, \dots, 15\sigma$ transitions where 1σ is $0.257 \text{ Jy beam}^{-1} \text{ km s}^{-1}$. We primarily see disk A, and can see that its eastern side (in red) is receding from us while its western side is approaching us. Disk B is largely invisible in the CO line, but we can see its influences in the spread of (blue) emission on the map's western side. | 37 |
| 3.7 | A PV diagram of disk A's HCO^+ emission. Some asymmetries are readily noticeable. | 38 |
| 4.1 | Since disk A and B's features are assumed to be independent, we may generate corner plots for each of their parameter spaces individually. Some analysis. REWORK: these are not the most recent ones | 48 |
| 4.2 | Cornerplots of results from MCMC fitting of HCO^+ emission. | 55 |
| 4.3 | Channel maps of HCO^+ emission data, as well as a best-fit model from MCMC fitting and residuals from the two. | 56 |

| | | |
|-----|--|----|
| 4.4 | Moment-1 map of HCN emission, overlaid with ellipses described by each disk's best-fit position angle, inclination, and outer radius. For disk B, both the best-fit outer radius with and without the 220 AU a posteriori prior implemented (at 324 and 145 AU, respectively) are plotted. | 57 |
| 4.5 | Cornerplots of results from MCMC fitting of HCN emission. | 58 |
| 4.6 | Channel maps of HCN emission data, as well as a best-fit model from MCMC fitting and residuals from the two. | 59 |
| 4.7 | Cornerplots of results from MCMC fitting of HCN emission. | 60 |
| 4.8 | Channel maps of CO emission data, as well as a best-fit model from MCMC fitting and residuals from the two. | 61 |
| 4.9 | Density and temperature profiles for the best-fit models for CO, HCO ⁺ , and HCN. | 62 |
| 5.1 | Models showing radial and vertical distributions of CO, HCO ⁺ , and HCN in a simulated disk around a T-Tauri star. The top row shows the profiles of isolated disks (Walsh et al. 2010), while the bottom row shows the profiles of disks being irradiated by a nearby O star (Walsh et al. 2013). Note that bottom row is on a log scale and only covers the inner 100 AU of the disk, while the top row is linearly scaled and shows a 300AU stretch. <i>It seems like only having one of these sets of images would make more sense.</i> | 68 |
| 5.2 | Some stuff from Eisner2018. | 70 |

Chapter 1

Introduction

Planetary systems, including our own Solar System, are born from circumstellar disks of gas and dust around young stars. Young ($\leq 10\text{Myr}$) circumstellar disks, known as protoplanetary disks, are easily distinguishable from their older siblings by their large abundance of gas, which typically outweighs the disk's dust by a factor of 100. However, as these disks age they are influenced by gravitational, chemical, and viscous forces, and their gas almost entirely dissipates as they become debris disks, much like our familiar local Solar System's Kuiper Belt and asteroid belt. But while we can observe with relative ease the current state of our local planetary system and debris disks, understanding the process that brought us here is much more difficult. To do so, we must understand the nature of our own disk at its birth, and whether or not that process is a common one that we would expect to see replicated elsewhere. Unraveling this mystery requires that we turn to observations of other comparable protoplanetary disks in order to develop a coherent narrative of disk evolution and, consequently, the conditions necessary for the formation of planetary systems like our own.

To understand the birth of our protoplanetary disk, we must understand the birth of our Sun, as the two are intimately related. Stars form when a region of a molecular cloud develops a gravitational instability sufficient to lead to a runaway collapse (F. Shu, F. Adams 1987), helped along by macroscopic turbulence in the

cloud (McKee & Ostriker 2007). In this process, the cloud shrinks by a factor of around ten million on its way down to a star, analogous to shrinking a square the approximate size of Connecticut ($\sim 150 \times 150$ km) down to just 15mm on each side. Angular momentum, defined as the product of a system's mass, velocity, and radial extent, must be conserved throughout this process, leading to a tremendous increase in the collapsing cloud's angular velocity. As the local material begins to self-gravitate, its center forms a dense core which will eventually become a young star¹.

However, if that angular momentum is conserved only through an increase in angular velocity, those velocities will become so large that the star itself will be unable to form, as centrifugal forces pulling outward will become more significant than the gravitation pulling the star in on itself. In order to prevent velocities from becoming this high, stellar jets and disks, made from the collapsing material, will develop to decentralize the system's mass and dissipate its angular momentum.

The resulting disks present flared radial structures, typically extending several hundred AU (Vicente & Alves 2005). Since these disks form directly out of the collapse process, they, like their stellar host and the initial molecular cloud, are initially composed almost exclusively of molecular hydrogen, although their chemical evolution is significant and heavily studied². Temperatures in their outer reaches are typically in the range of 10-100 K; gas masses are inferred to range from ones to tens of Jovian masses (Andrews & Williams 2005), although this value comes with significant assumptions that are discussed in depth in §1.1.2. Masses for the disks in the present study are calculated in Chapter 3.

¹binaries are also a common outcome in this process; according to Duchêne & Kraus (2013), approximately half of all stars are found in binary systems.

²Improving our understanding of this chemical evolution is also one of the motivating drives of this thesis.

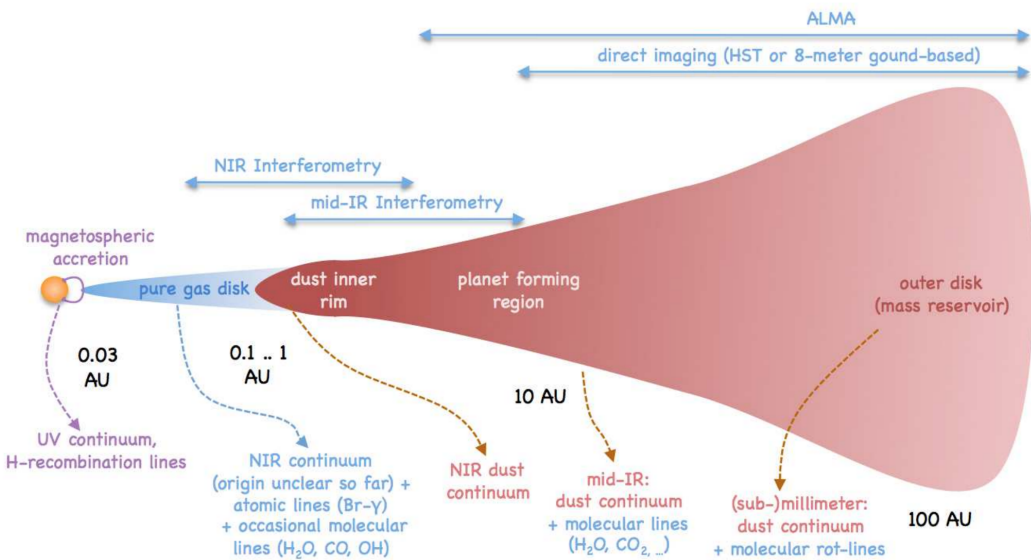


Figure 1.1: An edge-on slice of a protoplanetary disk is presented (Dullemond & Monnier 2010). As is visible in this graphic, significant radial segmentation of the disk exists, particularly between the inner gas disk and outer disk of gas, dust, and planetesimals. Also of note is the large vertical flaring that occurs at large radii. Since the observations that this thesis are based on were made with ALMA (discussed in §1.1.1), we are sensitive primarily to the outer reaches of the disk.

By around 10-20 Myr, the primordial gas and dust in these disks becomes depleted through several processes, including accretion onto the host star, blowing out from radiation pressure, and becoming locked up in icy bodies, transitioning the disk from a protoplanetary disk to a debris disk. These new debris disks are made up of what is thought to be second generation dust, created by the grinding down of boulders and planetesimals, since any primordial dust from the initial collapse should have been blown out by this time. The gas masses in debris disks tend to be orders of magnitude lower than in protoplanetary disks. For a more complete review of disk evolution, see Hughes et al. (2018).

1.1 Submillimeter Observations

Although protoplanetary disks' masses are dominated by gas, they still have sufficient dust to be optically thick in the optical. Consequently, mass measurements are not possible at optical wavelengths. However, since the optical depth of the dust at millimeter wavelengths is low, and since the emission being observed at these wavelengths is thermal rather than due to scattering (as it is in the optical), observations at millimeter wavelengths are preferred for measuring a disk's dust mass. In the radio, we may trace two types of emission:

- **CONTINUUM EMISSION:** Although the size distribution of grains in a dust disk is wide and heavily weighted towards smaller grains, larger, millimeter-sized grains are still present in disks. These larger grains are far more efficient emitters in the radio, since the wavelength of a grain's peak thermal emission efficiency is approximately equal to its size. Thus, we may observe this continuum emission (so named thanks to the wide range of frequencies that thermal emission covers) from these millimeter-sized grains.

- LINE EMISSION: Because radial disk temperatures quickly fall below the temperatures required to cause photodissociation, molecules may live a stable existence in these disks. Conveniently, the rotational transitions of small molecules tend to emit at radio frequencies. Observations of the emission from these rotational transitions, known as line emission, can provide us with a wealth of important information, including kinematics, temperature information, disk chemistry and total disk mass.

Notably absent in both forms is emission from the central star, thanks to the fact that stars are extremely weak emitters in the radio regime, since stars are hot and, consequently, have peak emission in the optical³. This makes them very faint relative to the disk’s emission at longer (hundreds to thousands of microns) wavelengths. Fig 1.2 (Hughes 2010) presents a spectral energy distribution, or SED, showing emission intensity as a function of wavelength from an imaginary disk system, demonstrating how small the star’s flux density is at long wavelengths relative to the disk’s contributions.

However, to understand these types of observation, one must first understand the nature of the “telescope” making the observations. What follows is a brief introduction to radio interferometry, followed by more complete explanations of continuum and line emission.

1.1.1 Interferometry

Interferometry is a clever way to make extremely high-resolution observations at long wavelengths without needing to use incredibly large collecting areas. Were

³Why, then, is the dust still bright relative to the star? While it’s true that the flux *per area* of the dust is significantly smaller than of the star, the dust has a far greater surface area, allowing it to compensate and still be a bright emitter.

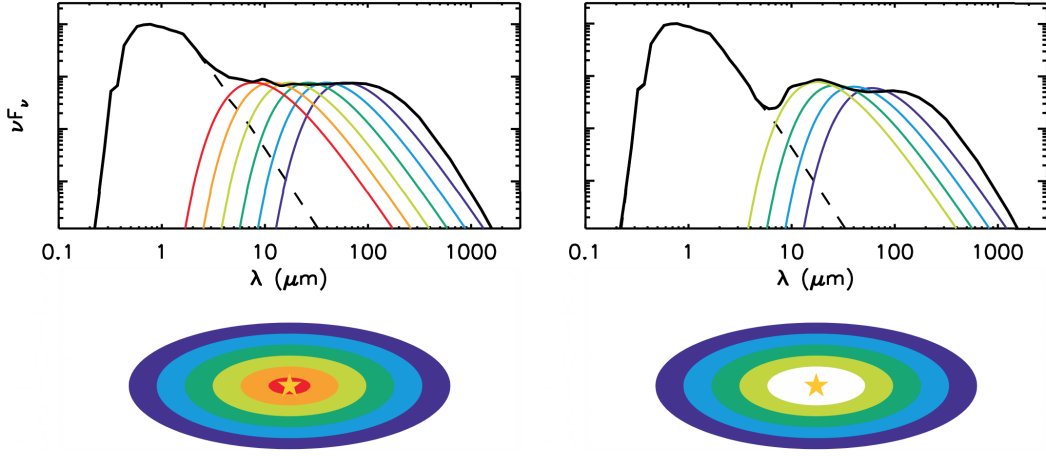


Figure 1.2: Two example SEDs, accompanied by cartoon models to illustrate the various contributions of different elements of a disk and their influences on the SED (Hughes 2010). The dashed line corresponds to emission from the stellar photosphere, while the colored lines are blackbody curves corresponding to emission from regions of the disk with different temperatures. Since radio observations take place at longer (hundreds to thousands of microns) wavelengths, one may easily see that the stellar contribution in that regime is minimal.

one to naively attempt to create a “traditional” (single-aperture) telescope to capture radio emission, they would quickly recall that, for a telescope with a single circular aperture of diameter D , maximum angular resolution is given by

$$\theta = 1.22 \frac{\lambda}{D}, \quad (1.1)$$

where θ is the angular resolution achieved, and λ is the wavelength of the emission being observed. Unfortunately, light in the radio regime has wavelengths on the order of millimeters to centimeters, orders of magnitude longer than optical light, which is in the hundreds of nanometers. Consequently, to achieve a resolution comparable to that of an optical telescope, one would have to increase their aperture’s diameter accordingly to match the increase in λ . Some have tried this approach: the Arecibo Observatory in Puerto Rico and the Five hundred

meter Aperture Spherical Telescope in China (with diameters of 300m and 500m, respectively) are two immediate examples, but both still have resolutions ($\sim 25''$ for Arecibo and $\sim 15''$ for FAST, observing 3cm emission) that are too coarse to resolve the length-scales that we would like when observing disks. Building and maintaining apertures this big is also an extreme challenge, usually requiring mountains to be hollowed out, making this an unappealing solution.

The alternative is to leverage the power of interferometry for a solution to the problem. In an interferometric system, one may construct an image using the interference patterns between light received by two or more separate apertures. In this case, the maximum angular resolution becomes inversely proportional to the maximum distance, or *baseline*, between any two apertures, which can be made almost arbitrarily large. Interferometry does come with tradeoffs, however, the most notable of which is in sensitivity, since sensitivity is proportional to collecting area and each dish in an interferometer is typically fairly small. Additionally, interferometers also have inherent spatial filtering, meaning that they are not sensitive to flux from sources covering large angular scales. This is because the largest angular scale of a flux source that a telescope is sensitive to is inversely proportional to its smallest baseline. Since the collecting area of a single-dish telescope is a continuous surface, its smallest “baseline” is essentially infinitely small (making it sensitive to arbitrarily-large flux sources). Conversely, for an interferometer, that smallest baseline is typically ones to tens of meters. Therefore, interferometers are intrinsically unable to capture flux from sources with angular scales larger than λ/D_{\min} .⁴

While this interference process can be done at optical wavelengths with CCDs,

⁴This can actually be an advantage, however, as it offers the opportunity to choose the length-scale being observed, i.e. remove cloud contamination (large scale structure) from an image of a disk (a small structure).

it is far more difficult to execute, as light must be forced to physically interact before reaching the sensor via a complex and extremely precise optical system. At longer wavelengths, however, heterodyne receivers may be used, making the task of interfering the signals a digital process, rather than a physical one. A heterodyne receiver records both the amplitude (analogous to the intensity that a CCD might measure) and the phase of the signal it receives. Because the receiver captures phase information as well as amplitude, the signals from two dishes may be digitally interfered after being received. Physical features must be calibrated out, including phase delay caused by differences in line-of-sight path length from the source between the receivers, atmospheric effects, and instrumental phase delays. The result, for a single baseline, is a complex voltage pattern describing the amplitude and phase of the interference pattern between the signal each dish received. We call this voltage pattern a *visibility*.

The complete output from an interferometer is a collection of these visibilities. Taken together, they approximate the Fourier transform of the sky image. We say that this output lives in the “visibility domain”, which itself is a Fourier transform of the image domain. A single visibility relates to the full set of visibilities analogously to the relationship between a pixel and an image.

While the image domain has spatial dimensions (i.e. the xy plane), the visibility domain instead uses the uv plane. The uv plane is a wavelength-scaled $x - y$ coordinate system parallel to the sky in the direction of the target source. Here “wavelength-scaled” can be taken to mean that $u = X/\lambda, v = Y/\lambda$, where λ is the wavelength of observation and X and Y are the lengths of the x and y (i.e. north/south, east/west) components of the projected baseline. Thus, each baseline samples a specific spatial frequency, given by $\theta = 1/\sqrt{u^2 + v^2}$. An interferometer may thus be represented on the uv plane as a scatter of points, with

each point corresponding to the wavelength-scaled, target-projected, component distance between two receivers. The ideal aperture would completely fill the uv plane, so that every spatial frequency was sampled. However, since the number of baselines we may access is very limited (approximately the square of the number of antennae in an array), this is clearly an impossibility for an interferometer.⁵

However, the fact that the *projected* baseline is really what determines visibility’s location in the uv plane, rather than the baseline’s “true”, un-projected length, allows us to cleverly gain far more points in the uv plane than one might immediately expect. Since the Earth rotates throughout the night, the projection of a given baseline relative to the target source will change throughout the night as well. Consequently, by making observations over the course of a night, many more points in the uv plane may be sampled, yielding a better-filled plane. This process is known as “Earth rotation aperture synthesis.”

We now consider how one might recover an image from a set of observed visibilities. In general, moving between frequency space and distance space is given by a simple Fourier transform. When applying this translation to telescopes, we consider the shape of the image produced by observation of a single point source directly on axis with the aperture. For a conventional telescope with a circular aperture, coverage in the uv plane is in the shape of a filled circle of constant amplitude. Translation to the image domain, via a Fourier transform of that shape, results in the familiar 2-D Airy Disk, the characteristic point-spread function (PSF) of a single aperture convolved with a point source. With an interferometer, this process would be equally straightforward if the uv plane were fully sampled, but because it is not, the resulting image is instead a Fourier

⁵Of course, a single-aperture telescope does not have this problem since its uv plane is one continuous collecting area and thus can be seen as having infinite baselines and complete uv coverage.

transform of all the points in the uv plane sampled by the baselines, and can take on a very complex shape⁶. However, while this shape is complex, it is still - as is the case in the optical - just a convolution of the point source with some PSF, only in this case the PSF is more complicated than an Airy function. As we increase the number of uv points sampled, the resulting image will increasingly approximate a bumpy and/or elongated Airy disk. In radio astronomy, we call this PSF the “dirty beam”.

When observing a source, we would like to find the true sky brightness pattern (i.e. the sky image). As described above, the Fourier transform of a set of visibilities is a convolution of the dirty beam with the true sky brightness pattern. Therefore, we would like to remove the dirty beam’s contributions to the image. The process of removing the influence of the dirty beam, and the artifacts it can introduce, is called deconvolution. In practice, this deconvolution process takes the form of some iterative algorithm that selectively removes the effects of the dirty beam. The curious reader is referred to the CLEAN algorithm (Hogbom 1974), the first and most popular deconvolution algorithm (and the one used in this work), as well as the maximum-entropy method (Wernecke & D’Addario 1977; Skilling & Bryan 1984). It is worth noting at this point, however, that due to the artifacting and non-unique result that the imaging process introduces, all of our analysis is performed directly on the visibilities themselves, rather than the image. This means that the specific parametrization of CLEAN or any other step in the imaging process does not need to be perfect, since it is purely diagnostic or expository.

⁶ Additionally, thanks to the incomplete sampling of the uv plane, an infinite number of images could all be consistent with some given finite set of visibilities, although many of them would not be physically possible. The one we choose to look at is determined by our deconvolution process, but is not actually the true image.

In summary, interferometry works by recording amplitude and phase information about some emission with many radio antennae and digitally interfering each antenna's signal with the signal received by every other telescope. Each of the resulting interference patterns is called a visibility, and represents a point in *uv* space. Translation from the visibility domain to the image domain involves taking the Fourier transform of the visibilities and deconvolving the dirty beam's influence.

Currently, the world's most advanced interferometer, and the source of this thesis's data, is the Atacama Large Millimeter/Submillimeter Array (ALMA), shown in Fig 1.3a. Built in the high Chilean desert at around 5,000 meters (16,000 feet), the \$1.4-billion array first opened its eyes for scientific observation in mid-2011, with funding from a global partnership between Chile, the United States, and several other countries. With its 66 total antennae (50 12-m dishes and 16 7-m dishes) and baselines extending out to 15-km, it offers an order of magnitude increase in sensitivity and resolution over previous arrays that observe at similar frequencies, which include the Submillimeter Array (8 6-meter dishes), NOEMA (10 15-meter dishes) and the CARMA (23 dishes of 3.5-m, 6.1-m, and 10.4-m diameters).

The effects of this increase are impressive; gaps and rings in faraway disks are now resolvable in striking clarity (Fig. 1.3b), providing a treasure-trove of opportunity to hone our understanding of disk evolution and planetary-system formation. ALMA has also been a blessing to other subfields of astronomy as well, enabling high-resolution observations of everything from complex organic molecules in disks (Walsh et al. 2016; Podio et al. 2019) to gravitational lensing from dark matter halos (Herrera-Martín et al. 2019) to molecular tori around black holes (Combes et al. 2018). Additionally, as a component of the Event Horizon

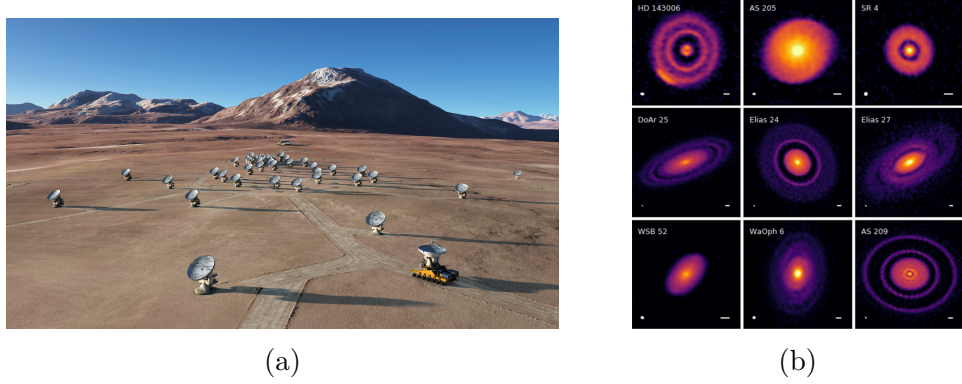


Figure 1.4: *Left:* A rendering of ALMA⁷ shows the interferometer’s antennae in the high desert, as well as a purpose-built truck moving one of the antennae (lower right). *Right:* A recent survey from ALMA by Andrews et al. (2018) reveals stunning detail in several protoplanetary disks.

Telescope, ALMA played a key role in imaging a black hole’s event horizon for the first time (Collaboration 2019). These awe-inspiring projects are a small portion of ALMA’s contributions to the world of radio astronomy, and more are being made with each passing day.

With an improved understanding of the mechanics of radio interferometry, we may now revisit continuum and line emission.

1.1.2 Continuum Emission

Continuum emission observations integrate flux from a wide band of frequencies, just as our eyes do in the optical. They are appealing for their simplicity and because, by integrating a wide band, they are sensitive to faint objects.

When observing protoplanetary disks, an understanding of planet formation is often a guiding motivation. One parameter that is critical to the planet-forming process is total disk mass. We know that, to first order, when a disk is optically thin, its total mass, M_{disk} , is linearly proportional to its flux density, F_{ν} (Hildebrand 1983), which is found from an observation of continuum emission. This

relationship is given by

$$M_{\text{dust}} = \frac{F_\nu d^2}{\kappa_\nu B_\nu(T_c)}, \quad (1.2)$$

where d is the source's distance, κ_ν is an assumed dust opacity, and $B_\nu(T_c)$ is the Planck function at a given characteristic temperature, T_c . The value of T_c and disk opacity can be inferred without much difficulty by fitting the disk's SED using a simple model. This function is, of course, rather approximate; it assumes a single temperature and single dust opacity (a function of composition and grain size distributions) throughout the disk. The assumption of optically thin emission means that calculations made will inherently be lower limits, since any substantial optical depth will block emission from inner regions of the disk. Furthermore, even in the case of optically thin emission, significant mass may be locked up in bodies that are invisible to our observations.

Traditionally, studies have used observed continuum fluxes to estimate dust mass and then inferred a total gas mass by assuming a 100:1 gas/dust ratio, based on the ratio observed in warm ISM clouds. However, an ALMA survey of 89 disks in Lupus tracing both continuum emission and two CO isotopologues (?Miotello 2017) found the true value of this value to be highly variable, often falling closer to 10 (Fig 1.5), and Liu et al. (2018) found that a ratio of 100 provoked instability (as measured by the Toomre criterion) in their smoothed-particle hydrodynamic simulation of the MWC 480 disk; instead, they found that values of 6-12 yielded their best results. *Could cite Bergin+ 2013 here for coming up with the HD stuff, but not sure how to make it work narratively.* In short, this ratio introduces a significant source of uncertainty, possibly of up to two orders of magnitude, into

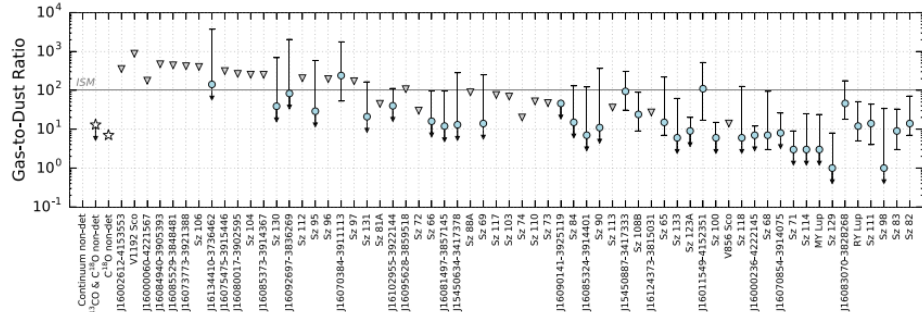


Figure 1.5: Gas-to-dust ratios in protoplanetary disks in Lupus (?). The ratio is highly variable and rarely best described by the canonical value of 100:1. Blue points indicate detections, and gray triangles indicate upper limits. Error bars with downward arrows indicate sources detected in ^{13}CO but not C^{18}O , for which the authors did not establish lower mass limits.

existing calculations of gas mass in protoplanetary disks based that are based on continuum emission.

1.1.3 Line Emission

As molecules collide with one another or absorb light, they gain energy, entering higher rotational energy states. However, as their presence in these states cannot be sustained without the addition of more energy, they will de-excite soon after. This de-excitation process - stepping down from one rotational energy state to the one below - causes the emission of light. Every transition in every molecule emits at its own specific frequency, or rest frequency, making that light identifiable to observers. We may observe a specific rotational transition from a single type of molecule by tuning our receiver to be sensitive to a very narrow window of frequencies immediately around the rest frequency of the transition of interest. This is known as a spectral window. The narrow range of frequencies at which a given molecular transition emits makes ALMA's large sensitivity particularly crucial for observations of molecular lines at high spectral resolution or in rare species.

One immediate feature that line emission gives us access to is velocity information: since all emission should have a single frequency (the transition's rest frequency), we immediately know that any variation from that central frequency is a result of Doppler shifting caused by line-of-sight velocity⁸. This allows us to make a “moment-one” map of emission, which shows the intensity-weighted velocity structure of the disks (Fig 1.6).

Observations of line emission also give us information about both the temperature and density structures of the disk, since these are the two factors that influence how much emission we observe. However, in the case of optically thin emission, the two are degenerate, since an increase in either one will increase emission intensity. In this case, we may combine observations of multiple species to model the temperature structure of a disk. In the case of an optically thick line, however, the temperature and density are no longer degenerate, since all emission originates from the $\tau = 1$ surface, which removes density from the equation and gives us a value for the temperature at that point in the disk's vertical structure. This is valuable, since the a disk's vertical temperature profile varies significantly, with the surface notably warmer than the midplane.

Besides offering information about radial density and temperature profiles, line emission also provides another way of finding total disk mass. Like the initial cloud that the star and disk formed from, the vast majority of the disk's mass comes in its gas, and like that initial cloud, the vast majority of that gas is molecular hydrogen, or H₂. However, since H₂ is a symmetric molecule and thus has no permanent dipole moment, it has no rotational transitions and does not emit in the radio, making it invisible to our instruments. As a consequence, we must

⁸Technically, the uncertainty principle tells us that a line will have some “natural” width, but this width is small compared to the Doppler width.

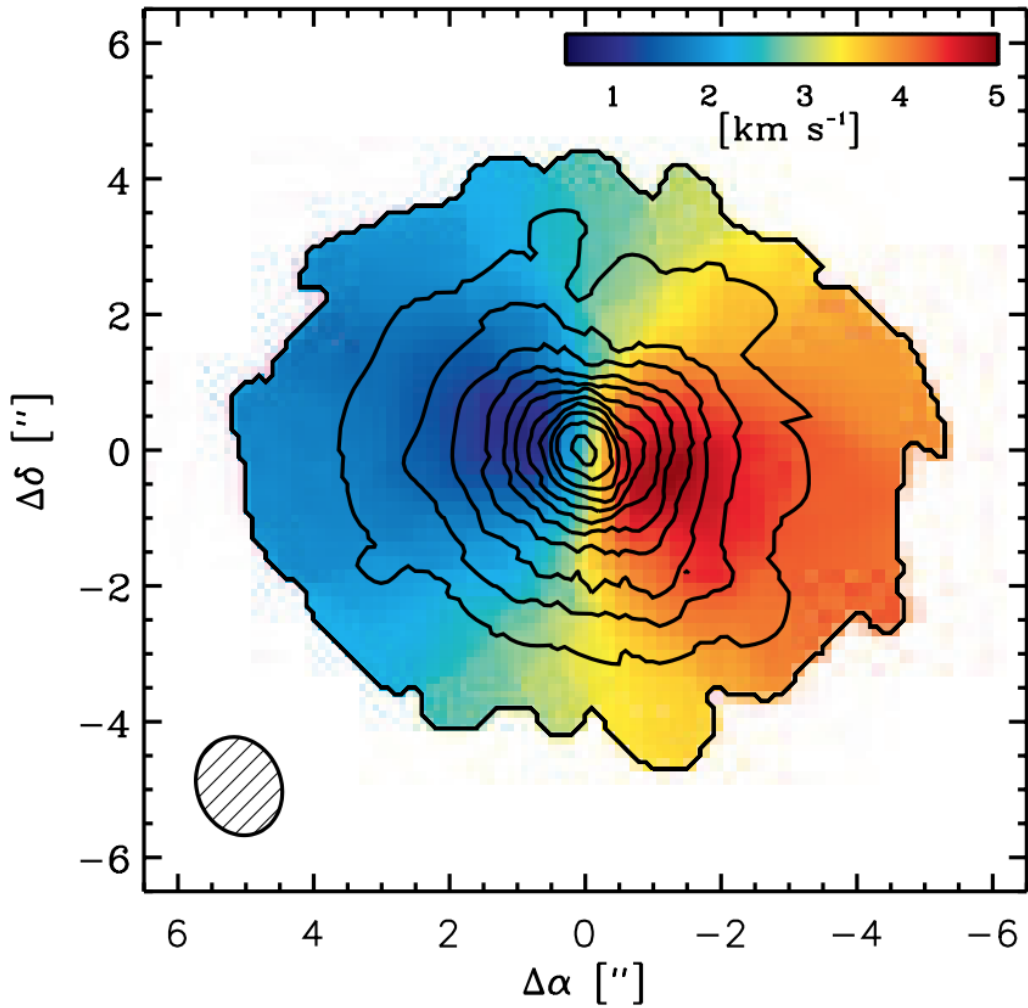


Figure 1.6: An example of a moment-one map of a protoplanetary disk, drawn from Rosenfeld et al. (2012). Colors correspond to intensity-weighted velocity; in other words, how quickly material is moving relative to the observer. One may consider this analogously to a spinning Frisbee, approaching the reader edge-on, where one half of the disk is spinning outwards (away from us) as the other side approaches. From this image, we immediately gain several pieces of information: for example, in this case, the disk as a whole is receding from view (since the velocity's "zero point", in yellow/green, is moving at 3 km/s), and that the disk's eastern half is spinning away from us, while the western half comes towards us. This gives us a quick understanding of the disk's kinematics.

instead observe emission from other molecules, make assumptions about those molecules' abundances relative to H₂, and extrapolate the total disk mass.

To do so, one generally begins with CO, second most abundant molecule behind H₂. Thanks to its abundance, as well as its relatively low excitation temperature, CO provides robust, bright emission. Drawing on measurements of CO/H₂ ratios in warm dense cloud (Aikawa & Herbst 2003; Fogel et al. 2011), we use a ratio of 1:10000, or 10⁻⁴, to represent CO's relative abundance in protoplanetary disks, while for other, more complex molecules, relative abundances are generally drawn the interstellar-medium literature and chemical modeling.

However, this CO/H₂ ratio of 10⁻⁴, which is frequently used to calculate total disk gas masses (e.g. Ansdell et al. (2017)) comes with significant uncertainty. Using a gas-grain chemical model Reboussin et al. (2015) showed, through an analysis of CO isotopologues, that at low temperatures (below 30-35K), CO is converted to less volatile molecules (typically s-CO₂ or s-CH₄). This means that below these temperatures, relative CO abundance quickly falls about two magnitudes below the literature value of 10⁻⁴. Schwarz et al. (2016) followed this modeling with high spectrospatial resolution ALMA observations of four CO isotopologues in the nearby protoplanetary disk TW Hya, and confirming a ratio of C/H₂ = 10⁻⁶. Additionally, Yu et al. (2017) notes that CO depletion in the outer disk and optically thick emission from the inner disk has lead observers (e.g. Ansdell et al. (2017), who found surprisingly low disk masses in their survey of ONC proplyds) to underestimate disk mass by more than an order of magnitude if they assume CO/H₂ = 10⁻⁴ and optically thin emission. They and Cleeves et al. (2015) also note that CO abundances change on short (~ 1 Myr) timescales, resulting in a degeneracy between disk age and mass. Ultimately, CO's tight dependence on disk temperature and its evolutionary trends with age increase

the need for a well modeled temperature profiles to inform the selection of an appropriate molecular abundance of CO.

1.2 Disks & The Role of Environment

There is significant evidence that most stars in our galaxy (Lada & Lada 2003; Mann et al. 2015), including our own Sun (Gaidos et al. 2009; Tachibana et al. 2006), formed in high-mass star forming regions, or HMSFRs. Therefore, understanding our own creation story necessitates the understanding of protoplanetary disk evolution in these SFRs, and the role that environment plays in that process. However, until ALMA came online in 2012, line-emission studies of disks in these HMSFRs were not feasible, due to the need for increased sensitivity and resolution in the observations.

Now that this telescope is available, however, HMSFRs are open for observation. We may use this opportunity to try to better understand the role that environment plays in the development and evolution of protoplanetary disks, comparing them to the well-studied disk population in low-mass (Andrews & Williams 2005; Mann et al. 2015) and the one well-characterized disk in an HMSFR (Factor et al. 2017), and evaluate how that environment may affect planet-formation potential.

1.2.1 The Minimum Mass (Extra-)Solar Nebula

The minimum-mass solar nebula (MMSN) is a conceptual aid used to inform astronomers about the distribution of material required to form a planetary system (Weidenschilling 1977). The MMSN is the radial mass profile that our own Solar System would present if the mass of each planet were, rather than being bound

up in spheres, instead ground up and spread across the ring bound by the orbits of their inferior and superior neighbors. Gas is then added to the ring until its gas:dust ratio reaches the canonical interstellar-medium value of 100:1⁹ (meaning that gas giants like Jupiter would have very little gas mass added, while terrestrial planets like Earth would have their mass significantly increased). The resulting mass profile represents the minimum surface density required to form our own protoplanetary disk and thus a way to inform our comparisons of other disks to our own. When this surface density profile is integrated into a single mass, it gives $M_{\text{MMSN}} = 0.01M_{\odot}$.

It is, of course, an extremely approximate characterization. One significant assumption it makes is that our planets formed in their current positions. This is a statement that we know both to be false (Walsh et al. 2011; Tsiganis et al. 2005) and consequential, since planetary migration can cause disks to lose mass by pushing competing planetesimals either out of orbit or into inner regions of the disk where they may be more susceptible to accreting onto the host star. Another assumption being made is that the chemistry is radially and temporally constant, which is also known to not be the case (van Dishoeck & Blake 1998).

The MMSN model was generalized to be tolerant to a wider diversity of planetary systems by Kuchner (2004) as the minimum-mass extrasolar nebula (MMEN), using 26 Doppler-detected planets in multi-planet systems to construct a disk analogous to that of the MMSN. Chiang & Laughlin (2013) developed a similar model, this time drawing on Kepler and HARPS planets ($n \approx 10^5$) to explain the existence of close-in ($P < 100$ days) super Earths, which make up approximately half of the planets observed in those catalogues. Both models assume that planets formed at or near their current positions. However, Raymond & Cossou (2014)

⁹This ratio is discussed more in §??

showed, using 191 multi-planet systems primarily drawn from the Kepler catalogue, that the resulting range of surface density profiles was broad, and thus that using a single, “universal” profile to locate disks with planet-forming potential - as the MMSN/MMEN purports to offer - was not plausible. They note that this broad spread likely reflected the necessity for consideration of planet migration, particularly amongst gas giants.

Still, while the MMSN clearly makes significant assumptions that lead to inconsistencies, it is nonetheless used as an approximate barometer for planet-forming potential.

1.2.2 Low- and High-Mass Star Forming Regions

Thanks to limitations in sensitivity and resolution, most submillimeter surveys in the pre-ALMA epoch focused on young disks in the nearby low-mass SFRs of Taurus-Auriga and ρ Ophiuchus. Dust-emission studies of disks in these regions by Andrews & Williams (2005, 2007) have yielded a wide range of disk masses, with a median of $0.005 M_{\odot}$ and a significant fraction with mass greater than the MMSN. This large fraction of disks with planet-forming potential is consistent with what we would expect based on the enormous - and still growing - number of exoplanets that have been discovered in the last two decades.

Of course, studying only nearby disks paints an incomplete picture of the population and its evolutionary trends; for one, most stars form in high-mass SFRs (Lada & Lada 2003; Mann et al. 2015), and low-mass SFRs are qualitatively different than their high-mass siblings. High-mass SFRs are massive, dense clusters with large abundances of high-mass O and B stars. Protoplanetary disks in these regions experience accelerated mass loss, thanks to the powerful ionizing radiation

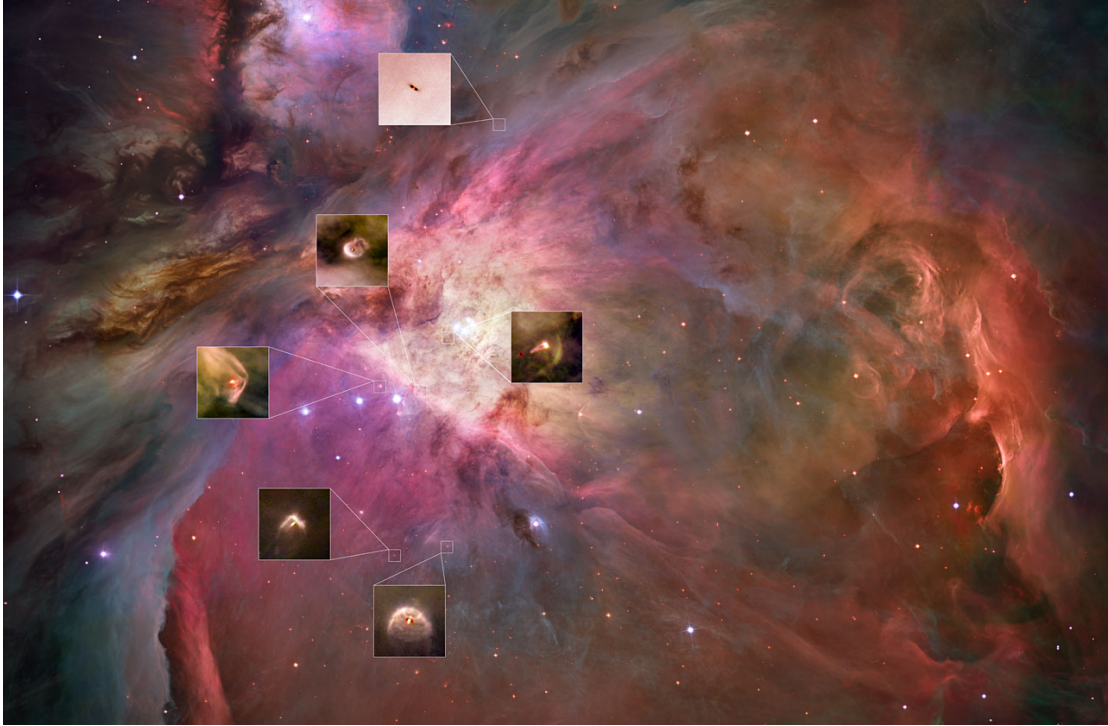


Figure 1.7: Proplyds in the Orion Nebula. The closer a proplyd is to a large, bright star, the more visibly windswept it is. Image courtesy of the Hubble Space Telescope Treasury Program on the Orion Nebula (Robberto et al. (2013))

from the high-mass stars (Anderson et al. 2013; Kalyaan et al. 2015; Xiao & Chang 2018). This mass loss is likely a problem for planet formation (Johnstone et al. 1998; Ovelar et al. 2012) and negatively affects potential habitability (Kruijssen & Longmore 2019), but its effects are not yet well understood. It is because of these factors that we would like to study disks in high-mass SFRs.

The nearest high-mass SFR to us is the Orion Nebula Cluster (ONC), 389 pc away. The Hubble Space Telescope was the first to dedicate significant time to the ONC, producing an abundance of iconic and awe-inspiring images the cluster and of the disks it hosts (Ricci et al. 2008). These studies have guided many subsequent observations, including many in the radio. Many of the cluster's protoplanetary disks (or proplyds, as those in the ONC are called) are visibly teardrop-

shaped, tailing away from the cluster’s biggest, brightest stars. Images like Fig 1.7, showing disks being pushed away from nearby bright stars, and countless others demonstrate the harsh environment that these young disks exist in. Indeed, the influence of these large stars has already been demonstrated, both in their affect on mass-loss rate and mass distribution. Statistically-significant anti-correlations between disk mass and proximity to the ONC’s central O star, θ^1 Ori C, have been shown using both data from the SMA (Mann & Williams 2009) and ALMA (Mann et al. 2014; Ansdell et al. 2017; Eisner et al. 2018).

Furthermore, both observations (Henney & O’Dell 1999) and modeling (Haworth et al. 2016) characterizing mass-loss rates for these proplyds in the Orion Nebula have found rates of $\dot{M} \approx 10^{-7} - 10^{-5} M_{\odot} \text{ yr}^{-1}$, implying that a typical disk (i.e. one of MMSN-scale, or $\sim 0.01 M_{\odot}$) should be fully dispersed before giant planets could form (Hubickyj et al. 2005) and before they could reach the inferred age of the disk-hosting stars in the ONC of ≈ 2 Myr (Reggiani et al. 2011).

Despite all this, not only do we still see disks, but we still see significant planet-forming potential in the Orion Nebula, potential that is comparable to that of other low-mass SFRs. A full 30% of disks surveyed in the ONC have disks with masses greater than or equal to the MMSN (Mann et al. 2014), falling comfortably between ρ Ophiuchus’ 29% Andrews & Williams (2005) and Taurus’ 37% (Andrews & Williams 2007).

However, since all these surveys are based exclusively on the analysis of dust continuum emission, the comparison is profoundly hamstrung by its reliance on assumptions of gas/dust ratios drawn from the ISM literature. This means that the resulting understanding of the gas masses in these regions is directly proportional to that 100:1 gas/dust ratio, a value that is almost certainly not accurate

(as discussed in §??). The consequences of this assumption are significant, since a disk’s gas mass directly determines its giant planet forming potential both by setting the amount of raw material available to the forming planet as well as by influencing the environment’s turbulence profile and planets’ migratory patterns within the disk. Furthermore, these continuum surveys cannot reveal these disks’ chemistries and the environmental influences that likely affect them, instead simply assuming solar composition. Together, these assumptions regarding both the total gass mass as well as its composition result in a heavy asterisk accompanying any claims we make about the birth and evolution of protoplanetary disks in high-mass SFRs. To solve this, we must understand the chemical make up of these disks, and for that we need studies of line emission.

Mann et al. (2014) made the first line-emission survey of the Orion proplyds as part of ALMA’s Cycle 0 Early Science operation. The survey studied 22 disks in four molecular lines (HCO^+ , HCN, CO, and CS) and $856\mu\text{m}$ continuum, and calculated each disk’s dust mass from the continuum emission. Since then, only one of the disks has had its line data analyzed. Factor et al. (2017) performed an analysis of the radial distribution of one of the disks’ gas by modeling emission from the lines to try to understand the chemical abundance and physical structure of different molecules in the disk. This fitting process was performed on three of the four molecular lines (as CS had insufficient signal to produce meaningful constraints).

In the study, the authors found several unexpected features: their measurement of the disk’s HCN abundance was higher than expected (although HCO^+ and CO abundances were consistent with literature values from low-mass SFRs), their mass measurement for the central star was inconsistent with the previously-determined spectral type, and they found a spatially unresolved high-velocity

excess emission feature in the HCO⁺(4-3) and CO(3-2) lines, with a positional offset from the central star. For this emission feature, they found that the source was blue shifted by -6.2 km s^{-1} relative to the systemic velocity, had a position consistent with a $60 \pm 20 \text{ AU}$ Keplerian orbit, and had an inferred H₂ mass of $1.8\text{-}8 \text{ M}_{\text{Jup}}$. They determined that the excess of emission was caused by a local density and/or temperature fluctuation in the inner disk, indicating that it was not a jet or cloud contamination. The authors propose that this could be the result of young Mars-sized bodies, collisions between particles trapped in mean motion resonance by a giant planet, magnetic-field-induced zonal flows, or planet formation.

These unexpected results demonstrate the need for further analysis of disks in this survey. The binary system that is the subject of this thesis is drawn from the same survey, representing the second and third ONC proplyds to have their temperature and density profiles characterized.

1.3 d253-1536: A Misaligned Binary System

The subject of this thesis is the system d253-1536, a binary of pre-main sequence stars in the M43 region of the Orion Nebula Cluster. Each star has its own proplyd. The stars' projected separation is somewhat atypically wide (approximately 400 AU), and their rotational axes are misaligned. Each star in the system has its own disk, henceforth called disk A and disk B (east and west, respectively, in all images of the system¹⁰).

¹⁰The reader will recall that this corresponds to disk A being on the left and disk B on the right of all images, since east and west are inverted in celestial coordinates relative to our familiar geographic ones.

1.3.1 Local Environment & Features

Many previous surveys have studied disks in the famous M42, or Orion Nebula, which lies adjacent to M43, and particularly the Trapezium cluster, a region near M42's brightest star O-star θ^1 Ori C. Mann et al. (2014) found a statistically significant correlation between disk mass and distance from θ^1 Ori C in a study of 70 proplyds (Fig. 1.9), particularly within 0.03 pc of the star, where there is a lack of disks more massive than $3M_{\text{Jup}}$. These disks are also truncated in radial extent, with no disks extending out past 60 AU in this region (Eisner et al. 2018).

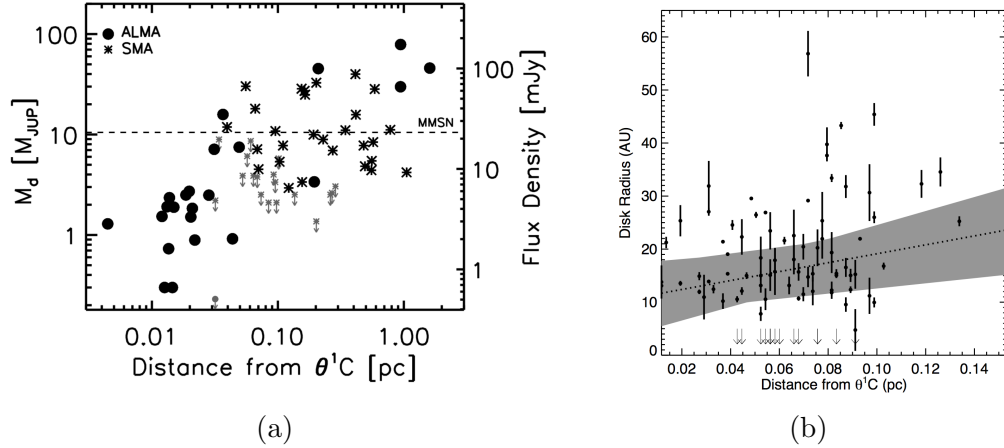


Figure 1.9: *Left:* The masses of 70 ONC proplyds are plotted against their projected distance from the Orion Nebula's central O-star, θ^1 Ori C, drawn from surveys from ALMA and the SMA (Mann et al. 2014). Grey markers indicate 3σ upper limits for non-detections. The dashed line at $10 M_{\text{Jup}}$ indicates the minimum-mass solar nebula. As is clear from this plot, a statistically-significant correlation was found between disk mass and distance from θ^1 Ori C. *Right:* Radius is also affected by proximity to θ^1 Ori C (Eisner et al. 2018)

However, because of M43's separation from the Trapezium cluster (it lies ≥ 1 pc to the cluster's north), disks in this region do not experience the same levels of photoevaporation. M43 has only one large emitter, ν Ori, which is a triple-star system whose main component is a B-type star. d253-1536 is wrapped in

an ionization bow shock, HH 668 A (1.10a), about $1''$ to the system's west and facing towards ν Ori, but otherwise the system shows no signs of influence from giant stars, whether in photoevaporation or in morphological influences (Mann & Williams 2009).

The misalignment of the disks' rotational axes is fairly typical of wide binaries like this one (Williams et al. 2014). The frequency with which these wide binaries present such misalignment indicates that wide binaries likely do not form in large, co-rotating structures, and emphasizes the importance of gas turbulence and interstellar interactions for young stars.

The system's larger disk, disk A, has a large jet emanating from it in observations in the optical made with HST (Smith et al. 2005). However, since the jet is not visible in the radio, we make no attempt to discuss, model or explain it.

1.3.2 Previous Observations

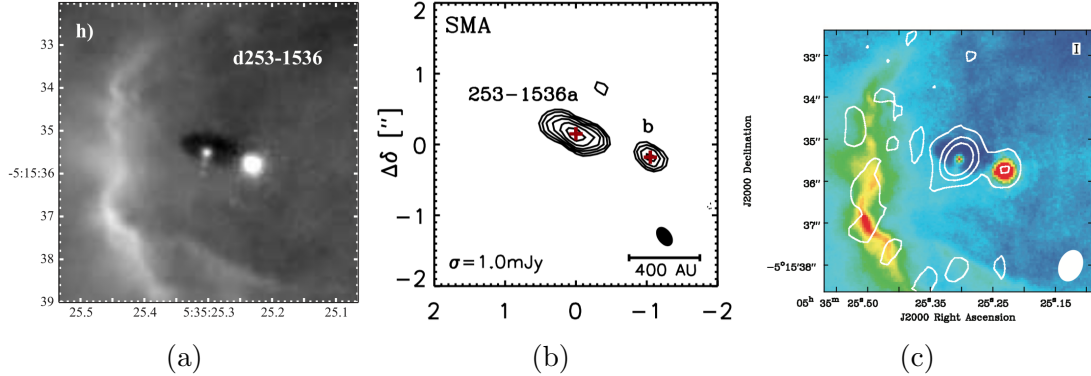


Figure 1.11: Images of V2434 Ori taken from Smith et al. (2005) on HST (Fig. 1.10a), Mann & Williams (2009) with the SMA at $880\text{ }\mu\text{m}$ (Fig. 1.10b), and Ricci et al. (2011) with the EVLA at 7mm (Fig. 1.10c). The ionization front is clearly visible in both the HST and EVLA observations, and the jet from disk A is visible in the HST image.

First observed by Smith et al. (2005) using the Hubble Space Telescope, the

authors took interest in what they saw as a binary system containing one star without a disk and one star embedded in a proplyd with a large jet and exhibiting tidal interactions with its companion (Fig 1.10a). Mann & Williams (2009) used 880 μ m continuum measurements to estimate dust masses of the disks to be 0.066 M_{\odot} and 0.018 M_{\odot} , for disks A and B respectively, making d253-1536a the most massive disk measured in the ONC, significantly larger than the Cluster's second largest disk at 0.034 M_{\odot} and adding credence to the theory that θ^1 Ori C is likely responsible for the truncation of disk masses in the Trapezium cluster. Subsequent detections at 7mm by Ricci et al. (2011) indicated that both disks are hosts to substantial populations of large dust grains (1.10c), although the distributions of grain sizes are different in the two disks. The same study also spectral typed the host of d253-1536b to be an M2 star and G2 for d253-1536a's host star.

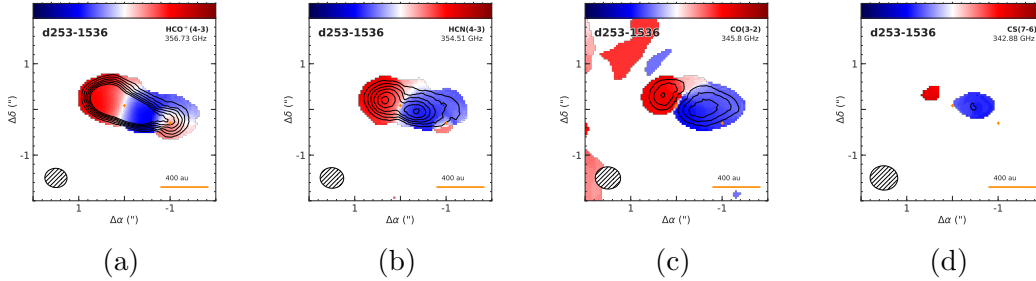


Figure 1.13: Moment-1 maps of HCO⁺(4-3), HCN(4-3), CO(3-2), and CS(7-6) emission (left to right) in the present study's proplyds, observed with ALMA's Band 7. Each map shows intensity-weighted velocity, which allows us to trace the disks' kinematics. REWORK: considering making this a 2x2 grid, instead of 4 across.

The system was observed in an ALMA survey of 22 proplyds in M43 by Mann et al. (2014) in four molecular lines (HCO⁺(4-3), HCN(4-3), CO(3-2), and CS(7-6); Fig ??), and preliminary fits of the system's kinematics in the HCO⁺(4-3) line were made by Williams et al. (2014). Using continuum observations alone and

assuming canonical values for temperature, dust opacity, and gas-to-dust ratio, they found disk masses of $0.074 M_{\odot}$ and $0.028 M_{\odot}$ for disks A and B, respectively, larger than the previous values. They found an inclination for disk A of $i_A \sim 65^{\circ}$, but did not resolve disk B and thus were unable to determine its inclination. They found systemic LSRK velocities of 10.55 and 10.85 km/s for the two disks, which are close enough to be well within the escape velocity that the authors calculated for a disks at their projected separation of 440 AU of 2.5 km/s, indicating that the binary is bound. This similarity in systemic velocity also indicates that the binary's orbital plane is likely close to face-on.

With our high resolution observations of gas line emission, we aim to determine the temperature, density, and chemical profiles of the system, as well as refining the mass estimates for both disks and host stars. With this information in hand, we will examine this disk's characteristics in the context of previously studied disks in the Taurus and ρ Ophiuchus star forming regions, as well as comparing it to the disk studied by Factor et al. (2017), and evaluate the disks' planet forming potentials.

1.4 Summary of Contents

In this work we characterize ALMA observations of two young protoplanetary disks in the d256-1536 system. Observations and data reduction are described in §2. In §3, data and basic analysis are presented. Descriptions of modeling and fitting techniques are discussed in §4, and in §5, best-fit parameters are discussed and contextualized, as well as unexpected features maybe.

Chapter 2

Observations

The data presented in this thesis are part of an ALMA survey of Orion proplyds in Orion (project 2011.0.00028.S); data collection and analysis methods of the continuum results are presented in Mann et al. (2014). The observations were taken on October 24, 2012, in ALMA’s Band 7 receivers. Four spectral windows of width 1.875 GHz were arranged to cover the rest frequencies of the $\text{HCO}^+(4\text{-}3)$, $\text{HCN}(4\text{-}3)$, $\text{CO}(3\text{-}2)$, and $\text{CS}(7\text{-}6)$ transitions (356.734 GHz, 354.505 GHz, 345.796 GHz, and 342.883 GHz, respectively). Each window was split into 3840 channels with a width of 488.28 kHz, yielding a velocity resolution of 0.42 km s^{-1} . Since this was part of a Cycle 0 Early Science project, the survey used only 22 of the ALMA’s 50 12 meter dishes in a hybrid configuration, with baselines ranging from 21.2 to 384.2 meters. This configuration yields a maximum angular scale of $8''$, angular resolution of $0.''5$, and beam FWHM of $15''$. At a Gaia-measured distance of 389 ± 7.97 (Gaia Collaboration 2016; Gaia Collaboration et al. 2018)¹, max angular scales and angular resolution correspond to 3,112 AU and 194 AU, respectively. The observation’s pointing center was (05:35:25.30, -05:15:35.50). Each disk’s precise position was fit for (see §4), and are given in Table 2.1.

These data, from Field 4 of Mann et al. (2014) represent 13.6 minutes of on-source time. This duration was split into six 136 second observations, spaced out over 7.5 hours to ensure adequate *uv* coverage, yielding an RMS of 7mJy/beam

¹This measurement is nearer than the previous literature value of 414 pc.

Table 2.1: Disk Positions

| Source | RA | Dec |
|---------------------|-------------------|-------------------|
| d253-1536a (disk A) | 05 : 35 : 25.3002 | -05 : 15 : 34.418 |
| d253-1536b (disk B) | 05 : 35 : 24.2940 | -05 : 15 : 35.800 |

in the line data. The resulting synthesized beam has dimensions of 0.57×0.51 arcsec with a position angle of 85° . Precipitable water vapor in the atmosphere was stable at 0.7 mm, indicating that atmospheric contributions to the data were negligible.

The data were calibrated by ALMA staff using standard procedures in the Common Astronomy Software Applications, or CASA (McMullin et al. 2007). The antenna-based complex gains and bandpass response of the system were calibrated using observations of the quasars J0607-085 and J0522-364 respectively. The absolute flux calibration was determined from observations of Callisto, using a model drawn from Butler (2012). Absolute flux calibration is estimated to be accurate to within $\sim 10\%$ (Mann et al. 2014).

The velocity reference frame was converted from CASA’s standard topocentric frame to LSRK (kinematic local standard of rest) using the CASA task `cvel`. Next, continuum emission was subtracted from the data in the uv plane using the CASA task `contsub`. Visibilities were imaged with standard inversion, deconvolution, and restoration procedures from the Multichannel Image Reconstruction Image Analysis and Display, or MIRIAD, package (Sault et al. 1995).

Chapter 3

Results

Spatially and spectrally resolved line emission was detected for CO (3-2), HCO⁺ (4-3), HCN (4-3), and CS (7-6) across around 50 channels with velocity resolution of 0.42 km s⁻¹. Here we present a discussion of these data, including line-emission statistics, diagnostic plots, and a consideration of the cloud contamination present.

3.1 Cloud Contamination

Cloud contamination occurs when emission from gas clouds along the observation's line of sight is detected. This is typically not a significant issue for observations of proplyds in low-mass star forming regions (SFRs), but since the Orion Nebula has a significantly higher gas density than those low-mass SFRs, cloud contamination presents problems in these data. This is particularly evident in the CO line, thanks to its low critical density and relatively high abundance in the background clouds, which allows it to excite and emit more readily than other molecules. As a result of higher critical densities and lower abundances, cloud contamination is less significant, but still present, in the other lines. It is crucial to manage and minimize the effects of this contamination before modeling so that our fitting algorithms do not try to model the cloud emission.

Luckily, there exist ways to minimize the effects of cloud contamination. To

do so, we take advantage of the fact that the contaminating clouds tend to be very large relative to a proplyds and that, as discussed in §1, interferometers have the ability to filter by length scale. Using these two features, we may exclude a selection of the shortest baselines used in our data, effectively shrinking the largest angular scales to which our receivers are sensitive and, consequently, significantly reducing the effects of the cloud emission without losing any information about our targets.

To characterize the cloud contamination in our images, we iteratively remove more and more of the shortest baselines from our data and measure the resulting RMS noise of an off-source area at each step. Were there no cloud contamination, this plot of RMS vs. min-baseline would trend upwards (following the fact that noise is typically proportional to the inverse square root of amount of data). However, we can recognize the signature of cloud contamination if we find unexpectedly high noise at low baselines that falls off at longer ones. This decrease reflects the fact that, since the clouds are large, only the shortest baselines are sensitive to their emission. This indicates that the ideal value to use as our minimum baseline length would be the inflection point at which the cloud contamination's contribution (decreasing with baseline length) gives way to the normal losses that come with decreasing signal (increasing with baseline length)¹. The results of making such plots are shown in Fig. ??.

From these plots, we find that excluding baselines less than $110 \text{ k}\lambda$, $80 \text{ k}\lambda$, and $60 \text{ k}\lambda$ for HCO^+ , HCN , and CO , respectively, yielded optimum results. Since emission from the CS line already has a very low SNR and a higher critical density

¹Another way to justify the removal of data is to recall that, not only are these short baselines recording too much cloud emission, but they are also generally not sensitive to the disks, since they are too small for these short baselines to pick up. Therefore, losing them effectively removes noise without any consequence to the data we really care about.

Table 3.1: Integrated Flux Measurements with Baseline Cuts

| Molecular Line | Baselines Included | Max Angular Scale (") | Integrated Line Flux (Jy km s ⁻¹) | |
|------------------------|--------------------|-----------------------|---|----------------|
| | | | Disk A | Disk B |
| CO (3-2) | All | 8."4 | * | * |
| CO (3-2) | > 60kλ | 3."4 | 2.58±0.47 | 1.85 ± 0.39 |
| HCN (4-3) | All | 8."2 | 0.80±0.07 | 0.26 ± 0.08 |
| HCN (4-3) | > 80kλ | 2."6 | 0.69±0.05 | 0.17 ± 0.08 |
| HCO ⁺ (4-3) | All | 8."2 | 5.79±0.49 | 2.29 ± 0.56 |
| HCO ⁺ (4-3) | > 110kλ | 1."9 | 4.15±0.31 | 0.80 ± 0.22 |
| CS (7-6) | All | 8."5 | 0.024±0.02 | [no detection] |

* Integrated line intensity was not calculated for CO(3-2) before the baseline cuts, as the data were too contaminated to give meaningful results.

than the clouds can easily access, it showed minimal contamination and thus excluding baselines did not improve the observations. Image statistics resulting from these cuts are presented in Table 3.1.

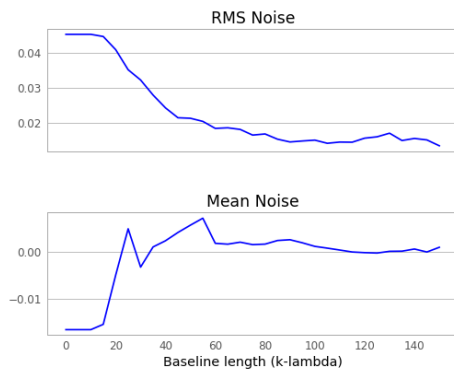
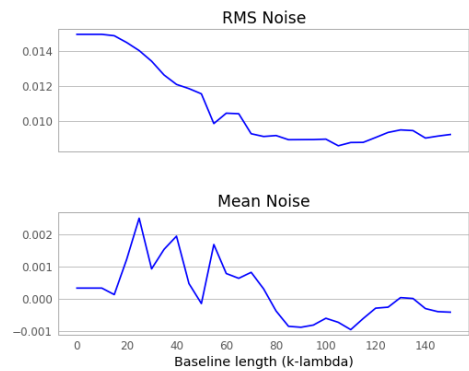
Figure 3.1: HCO⁺ Noise profiles

Figure 3.2: HCN Noise profiles

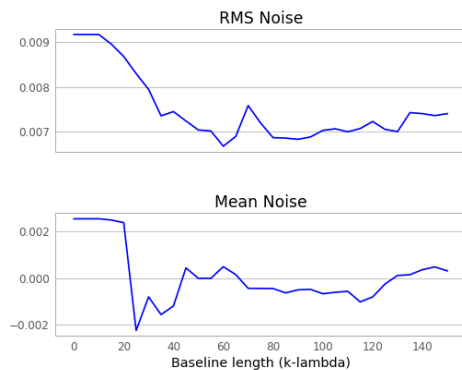


Figure 3.3: CO Noise profiles

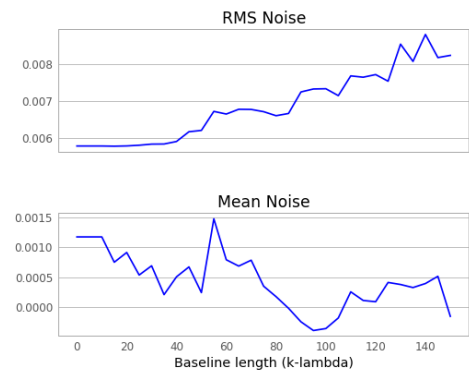


Figure 3.4: CS Noise profiles

3.2 Line Data

Integrated line flux was measured using the Miriad task `cgcurs` to measure the total flux in a zeroth moment map over the region enclosed by the 3σ contour. The results of these measurements are shown in 3.1. From these values, we may estimate the disks' gas masses.

Assuming optically thin emission and Local Thermodynamic Equilibrium (LTE), the line-emitting gas mass, M_{gas} is given by:

$$M_{\text{gas}} = \frac{4\pi}{h\nu_0} \frac{Fmd^2}{A_{ul}X_u}, \quad (3.1)$$

where F is the integrated line flux, m is the mass of the emitting gas molecule, d is the distance to the source, h is the Planck constant, ν_0 is the molecular line's rest frequency, A_{ul} is the Einstein coefficient for the $(u - l)$ transition, and

$$X_u = \frac{N_u}{N_{\text{tot}}} = (2J_u + 1) \frac{\exp[-B_0 J_u (J_u + 1) hc/kT_{\text{ex}}]}{kT_{\text{ex}}/hcB_0}. \quad (3.2)$$

In Eqn. 3.2, $\frac{N_u}{N_{\text{tot}}}$ is the ratio of the number of molecules in the upper state to the total number of molecules; the values used for this measurement and descriptions of them are given in Table 3.2. Since Eqn. 3.1 is the mass of the observed gas species, it must be scaled by the its relative abundance (fit for in Section 4) to obtain a total mass (*I'm not totally clear on this*). From this, we find a total mass of $0.x \pm 0.y M_{\odot}$.

We now turn to visualizing our data. Since line emission has a third (spectral)

Table 3.2: Values Used in Gas Mass Calculation (for HCO⁺(4-3))

| Parameter | Value | Description | Source |
|--------------------------------------|-------|-------------------------------|----------------------------------|
| F (Jy km s ⁻¹) | 4.15 | Integrated line flux | 0 |
| J | 4 | Quantum number of upper level | - |
| A ₄₋₃ (s ⁻¹) | 0.363 | Einsten A coefficient | Schöier et al. (2005) |
| E ₄₋₃ (cm ⁻¹) | 29.75 | Energy of 4-3 transition | Schöier et al. (2005) |
| B ₀ (hc) | 18.7 | Rotational constant | 1 |
| T _{ex} | 100 | Excitation Temperature | 2 |
| d (pc) | 389 | Distance | Gaia Collaboration et al. (2018) |

⁰ Calculated with MIRIAD task `cgcurs`

¹ $B_0 = \frac{2\pi E_{4-3}}{hc} \rightarrow B_o(hc) = 2\pi E_{4-3}$ (the formula for converting an electromagnetic wave's energy into a wavenumber.) **This is wrong still!**

² We approximate the excitation temperature to be the atmospheric temperature, which is valid in the case of optically thin emission and something else.

dimension, visualizing it presents a unique opportunity and challenge. Here we present our data, using a few of the more popular methods.

Moment maps offer us an intuitive way to flatten the three-dimensional data-cube (in α, δ, v) into two dimensions. Moment 0 maps integrate flux along the velocity axis as a function of position, providing insight into structures of emission intensity in the disk's morphology (while essentially sacrificing the data's spectral information), while moment 1 maps, a velocity-weighted intensity integration across position, tell us about a source's velocity gradients. Figures 3.5 and 3.6 show zeroth- and first-moment maps, respectively, of the CO line emission, with and without a 60 k λ baseline cut made (left and right, respectively).

With moment maps, we flatten through the velocity axis, but we can also flatten through the spatial dimensions as well using a position-velocity diagram (PVD). PVDs allow us to directly observe the velocity dispersion along a given axis in the image; usually this is a disk's major axis. In Fig. 3.7, we show a PVD of disk A's HCO⁺emission. In it, we see some noticeable asymmetry, both

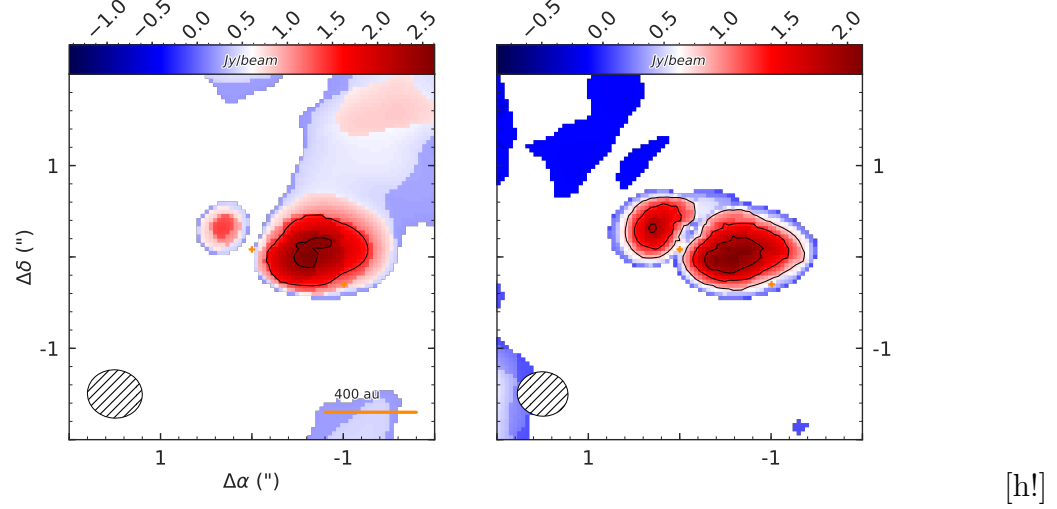


Figure 3.5: Zeroth moment map of CO emission, with and without a cut of all baseline's below $60 \text{ k}\lambda$ (left and right, respectively). Colors correspond to velocity-integrated intensity, while contours represent $\pm 3, 5, 7\dots 15\sigma$ transitions where 1σ is $0.257 \text{ Jy beam}^{-1} \text{ km s}^{-1}$. Negative contours are dashed. The beam is shown in the bottom left corner, with a diameter of $0.^{\circ}5$ which corresponds to 200 AU at 389 parsec.

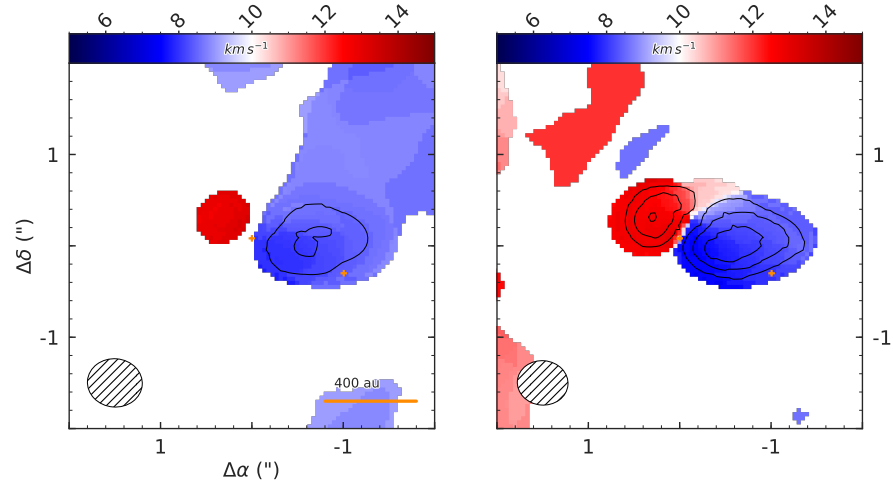


Figure 3.6: First moment map of CO emission, with and without a cut of all baseline's below $60 \text{ k}\lambda$ (left and right, respectively). Colors correspond to intensity-weighted LSRK velocity, while contours represent $\pm 3, 5, 7\dots, 15\sigma$ transitions where 1σ is $0.257 \text{ Jy beam}^{-1} \text{ km s}^{-1}$. We primarily see disk A, and can see that its eastern side (in red) is receding from us while its western side is approaching us. Disk B is largely invisible in the CO line, but we can see its influences in the spread of (blue) emission on the map's western side.

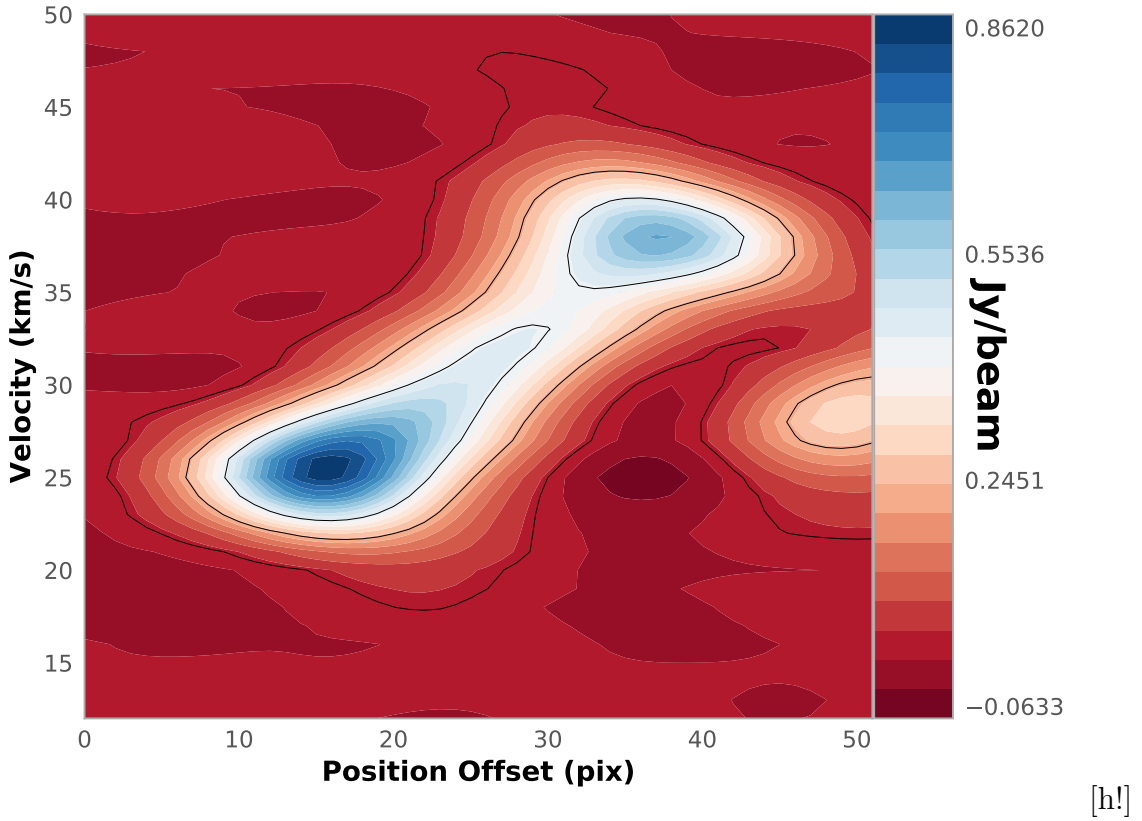


Figure 3.7: A PV diagram of disk A's HCO^+ emission. Some asymmetries are readily noticeable.

in terms of centroid intensity and in the extra feature at the eastern side of the map, which is likely the tail of disk B.

I don't know how valuable these PV diagrams are - is just having this one, of one disk in one emission line, sufficient, or should I make them for both disks in HCO^+ /both disks in all lines/something else? At this point, they're fairly easy to make, so the main cost would just be clutter.

Chapter 4

Analysis

By modeling spatially and spectrally resolved observations of protoplanetary disks, we can measure their chemical and physical characteristics. To model the system, we generate a synthetic image of what a disk with known characteristics (like disk radius, mass, chemical abundances, and so on) would look like at a certain distance, inclination, and position angle relative to us. We can then turn that synthetic image into a synthetic visibility set, and then compare those visibilities to our observations. By iterating this process and varying the value of those input parameters, we are able to generate many models with different parameter combinations, evaluate how well each resulting model disk matches our observations, and find which values best describe our disks.

In §4.1, we describe the basic equations and computational processes that generate the model disks. In §4.2, we describe how, once models are made, we move through high-dimensional parameter space to identify regions of best-fit. Finally, in §4.3, we present the results of our fitting procedures.

4.1 Gas Model

In this work, we use a gas-disk model originally developed by Rosenfeld et al. (2012, 2013) and translated from IDL to Python by Flaherty et al. (2015). The

code assumes that Local Thermal Equilibrium¹ (LTE), and hydrostatic equilibrium. The code draws on temperature- and surface-density profiles provided by the user to calculate a vertical density structure, and calculates the model disk’s velocity field based on the stellar mass. It then performs radiative transfer on the resulting structure to create a sky-projected image of the model disk, taking into account thermal and turbulent line broadening. The assumption of LTE allows the code to run quickly enough to allow for a Markov Chain Monte Carlo routine to generate models on a reasonable timescale, as described in §4.2.2.

4.1.1 Establishing Physical Profiles

A circumstellar disk can be characterized by three major profiles: its radial and vertical temperature structures, its radial and vertical density structures, and its velocity field. Generating a model disk is a matter of defining these three functions.

For the disk’s temperature profile, our code uses the parametrization of disk temperature structure first laid out by Dartois et al. (2003), where the disk’s temperature is given by,

$$T_{\text{gas}}(r, z) = \begin{cases} T_a + (T_m - T_a) \left[\cos \frac{\pi z}{2z_q} \right]^{2\delta} & \text{if } z > z_q \\ T_a & \text{if } z \leq z_q(r). \end{cases} \quad (4.1)$$

δ , a tunable exponent controlling the rate of the disk’s vertical temperature decay, is set to 1 as in Factor et al. (2017), though it can take on values between 1-2

¹This may or may not be a valid assumption in protoplanetary disks, but Pavlyuchenkov et al. (2007) showed that it was appropriate for CO.

(Dartois et al. 2003). The atmospheric temperature and mid-plane temperatures are given by $T_a = T_{\text{atm},150}(r/150\text{AU})^q$ and $T_m = T_{\text{mid},150}(r/150\text{AU})^q$, where q is typically negative and controls the functions' decay. Since T_m is smaller than T_a , the second term of the low-scale height temperature function is negative, so the sinusoid effectively implements a decreasingly-negative contribution to the temperature with height above midplane. The disk's scale height, controlled by z_q , is assumed to be radially increasing, as described by a power law, $z_q(r) = z_{q,150}(r/150\text{AU})^{1.3}$.

The disk's velocity field is assumed to be Keplerian with slight corrections for gas pressure support and the addition of a vertical dependence. The assumption of Keplerian velocities is generally valid in the case that $M_{\text{disk}} \ll M_{\star}$, which continuum observations of the system have shown to be the case for these disks. With these corrections added, the model disk's velocity field is given by

$$\frac{v_{\phi}^2}{r} = \frac{GM_{\star}r}{(r+z)^{3/2}} + \frac{1}{\rho_{\text{gas}}} \frac{\partial P_{\text{gas}}}{\partial r}; \quad v_r = v_z = 0. \quad (4.2)$$

The final structure we would like to define is the disk's gas density profile. By assuming hydrostatic equilibrium, we may relate the disk's gas density and temperature profiles as

$$-\frac{\partial \ln \rho_{\text{gas}}}{\partial z} = \frac{\partial \ln T_{\text{gas}}}{\partial z} + \frac{1}{c_s^2} \left[\frac{GMz}{(r^2+z^2)^{3/2}} \right]. \quad (4.3)$$

Here c_s is the local sound speed, given by $c_s^2 = \frac{k_B T_{\text{gas}}}{\mu m_H}$, T_{gas} is the temperature profile given above, m_H the mass of hydrogen, and μ is the mean molecular weight

of the gas, set here at 2.37 to reflect the gas's 80% H₂ composition. We may solve this equation by integration, giving us the disk's density profile $\rho(r, z)$.

The model's surface density profile is drawn from Hartmann et al. (1998), in which they expanded on the work of Lynden-Bell & Pringle (1974) to show that the structure of an isolated disk with viscosity given by $\nu \propto R^\gamma$ is well-described by

$$\Sigma_{\text{gas}}(r) = \frac{M_{\text{gas}}(2 - \gamma)}{2\pi R_c^2} \left(\frac{r}{R_c}\right)^{-\gamma} \exp\left[-\left(\frac{r}{R_c}\right)^{2-\gamma}\right], \quad (4.4)$$

where R_c is the radial extent of the gas disk, γ is a power law index, and M_{gas} is the total gas mass. This form allows the disk to behave as a power law radially until R_c , at which point it turns over into exponential decay. Hughes et al. (2008) showed that exponentially tapering the disk's outer radius, rather than sharply cutting it, provides the best agreement between gas and disk outer radii. We approximate $M_{\text{gas}} = M_{\text{disk}}$, since at this early stage in the disk's development, the gas is by far the majority element of the disk's mass total (although, as discussed in §1, this assumption has come under scrutiny in recent years).

Modifications are made to this density profile in two cases. At sufficiently low temperatures, molecules will condense out of the gas phase. The mid-plane of the disk is sufficiently cold to prompt this behavior. We simulate this behavior by dropping the gas density by a factor of 10^{-18} wherever the temperature falls below some characteristic freeze-out temperature, T_{FO} , a temperature which is molecule-specific. Conversely, at the disk's upper surface, photodissociation by stellar and interstellar radiation dominates, so we implement a decrease in density wherever the hydrogen column density at the disk's surface falls below a characteristic value.

Table 4.1: Molecule-specific values

| Parameter | Description | Fixed Value(s) | | |
|--------------------------------------|----------------------------------|----------------|------------------------|------------------------|
| | | CO | HCO ⁺ | HCN |
| T _{FO} (K) | Molecular freeze-out temperature | 19 | 60 | |
| σ _{Max} (cm ⁻²) | Column density upper limit | | 1.3 × 10 ³⁰ | 9.5 × 10 ²¹ |

* Values drawn from Factor et al. (2017)

We use values drawn from Factor et al. (2017) for these parameters, presented in Table 4.1.

4.1.2 Generating a Model Image

Having now established our model disk's physical structure through temperature, density, and velocity profiles, flux contributions through the disk are calculated. To do so, we find specific intensity by integrating the equation of radiative transfer:

$$I_\nu = \int_0^\infty K_\nu(s) S_\nu(s) e^{-\tau_\nu(s)} ds, \quad (4.5)$$

where $K_\nu(s)$ is the absorption coefficient, $\tau_\nu(s)$ is the optical depth and is defined as $\tau_\nu(s) = \int_0^s K_\nu(s')ds'$, and $S_\nu(s)$ is the source function. Since disks emit as blackbodies, the Planck function, $B_\nu(T)$, is used as the source function. Line broadening, a function of temperature and disk turbulence, is added, and the resulting flux is Doppler shifted to account for the disk's user-specified systemic velocity. Finally, the image is scaled, shifted, and rotated to account for the source's distance (d), angular offset from the center of the image ($Δα$ and $Δδ$), and position angle and inclination (PA and i) relative to our viewing direction.

Since the model disk is fully defined at every point in both physical and velocity space, we may set the spatial and spectral resolution to ensure that it is sampled well compared to the resolution of the data. We set our spectral resolution to match that of our observation, while we let the spatial resolution be $\sim 1/10$ the size of the synthesized beam. This resolution is high enough to avoid sampling artifacts when we simulate interferometric observations of the image.

We then use the Miriad task `uvmodel` to generate visibilities from the model image, sampled in the same *uv* tracks as our observation. The χ^2 statistic is then used as a goodness-of-fit metric to compare the data and model in the visibility domain. We make this calculation in the visibility domain, rather than the image domain, so that the resulting χ^2 value is not influenced by artifacts generated in the imaging process.

In summary, we can generate a model disk by calculating its physical structures (in radial temperatures, densities, and velocities), then drawing on radiative transfer to calculate the flux contributions from the disk. That flux is sky-projected to match the observed source's orientation, and the resulting image is then transformed from the image domain to the visibility domain and its fit quality evaluated.

4.2 Exploring Parameter Space

Now that we have the tools available to generate synthetic images that are tuneable across a large number of parameters, we must decide how best to move through that large parameter space to find a best-fit region. To do so, we use two methods.

4.2.1 Grid Search

The first, and perhaps most intuitive, way to move through this parameter space is using a simple grid search. A grid search involves manually assembling lists of values to try for each parameter and then generating models and calculating the resulting χ^2 value for every possible combination of parameters in those lists. A best-fit value is recovered by simply finding the point in that n -dimensional grid that yielded the best χ^2 , and then either calling that position in parameter space a best-fit location or then defining a finer grid around that point and repeating the process until an acceptable resolution has been reached. Benefits of grid search include its relatively straightforward nature (and, consequentially, the relative simplicity of implementing it) and its usefulness as a diagnostic tool, since very specific regions of parameter space may be sampled with the manual entry of positions to test. However, its simplicity leaves room for improvement.

We used grid search to locate the disks in (α, δ, v) space. All other parameters were fixed at best-guessed values, then grids were run with resolutions sufficiently fine to meet the observations' spatial and spectral resolution. Grids for the disks' systemic velocities were centered at values found in Williams et al. (2014), while $\Delta\alpha$ and $\Delta\delta$ offsets were first approximated using the MIRIAD task `uvfit` to fit a Gaussian to each disk. The resulting centroids were used to center the grids for refinement.

4.2.2 Markov Chain Monte Carlo

Markov Chain Monte Carlo (MCMC) algorithms offer us a way to both sample the probability distribution of a high-dimensional parameter space (much like a grid search), but offers an improvement over grid search by yielding the pos-

terior probability distribution of each point, which allows us to characterize the uncertainty associated with each best-fit value with error bars. We use an affine-invariant formulation of the MCMC algorithm described by Goodman & Weare (2010) and implemented in the Python package `emcee` by Foreman-mackey et al. (2013).

MCMC routines sample the probability distribution of a given n -dimensional parameter space by deploying an army of “walkers.” Each walker begins at some initial position, evaluates the χ^2 value of that point, and then proposes moving to a new position in parameter space according to a Gaussian probability distribution centered at the current point and decaying with distance (so that nearer points are preferentially, but not necessarily, selected). The χ^2 value of this new position - or “step” - is then evaluated, and is either accepted (the walker moves to that position) or rejected (the walker remains where it is and repeats the new-step proposal process) with probability $p = \exp[(\chi_{\text{current}}^2 - \chi_{\text{new}}^2)/2]^2$. This function indicates that if the proposed step yields a better fit (a lower χ^2 value) than the current position, $p > 1$ and the step is accepted. However, if proposed step results in a worse fit, there is still a non-zero chance that the step is accepted, proportional to how much worse it is. This willingness to accept an increased χ^2 value allows the walker to avoid becoming trapped in local minima. The list of steps taken by each walker and their accompanying χ^2 values are compiled into the “chain” part of Markov Chain Monte Carlo. Goodman & Weare (2010) show that a walker’s desire to remain in near a certain position is proportional to that position’s local probability density, meaning that we may infer uncertainties in our fits from the density of walker steps taken in a region.

²In practice, we take the natural log of both sides of this equation, such that the quantity we are really evaluating is $\text{lnprob} = \Delta\chi^2/2$.

We may introduce boundaries to the parameter space explored by our walkers using “priors.” These priors are manually set, and allow us to restrict the walkers’ motions from entering regions that we know a priori to be implausible fits. Justifications for these constraints are either physical (e.g. a disk should not have a negative radius) or observed (e.g. both disks’ radii are clearly far less than 1000 AU). These priors may be either uniform, with hard cuts at their bounds (and returning $\text{lnprob}=-\infty$), or Gaussian, with preferential treatment given to walkers closer to the Gaussian centroid (a known value). For this work, we implement a Gaussian prior on each disk’s position angle in order to guide the search towards the values reported in Williams et al. (2014) but still allow it the flexibility to self correct if necessary. This prior takes the form of a contribution to the log likelihood function, such that:

$$\text{lnprob} = -\chi/2 - \ln \frac{1}{\sqrt{2\pi\sigma_{PA}^2}} \exp^{-\frac{\text{PA}^2}{2\sigma_{PA}^2}} \quad (4.6)$$

for each disk’s position angle, where σ_{PA} is the position angle uncertainty given by Williams et al. (2014).

We may visualize the results of the walkers’ journeys using corner plots. Corner plots allow high-dimensional space to be visualized in two dimensions by taking slices across each pair of axes and showing the density of samples drawn in that slice. In each of these slices, a perfectly certain fit would appear as a very tight, point-like Gaussian - the sample density around the best fit would be extremely high and low everywhere else, as the walkers quickly converged and remained on that best fit point - while conversely, higher uncertainties are shown by a wide spread of samples around the central point. Degeneracies between parameters can

be seen as streaks in these corner plots, showing that a change in one parameter produces a change in the other. Corner plots for Disk A and B in an HCO⁺ fit are shown in Figs 4.1a and 4.1b, respectively.

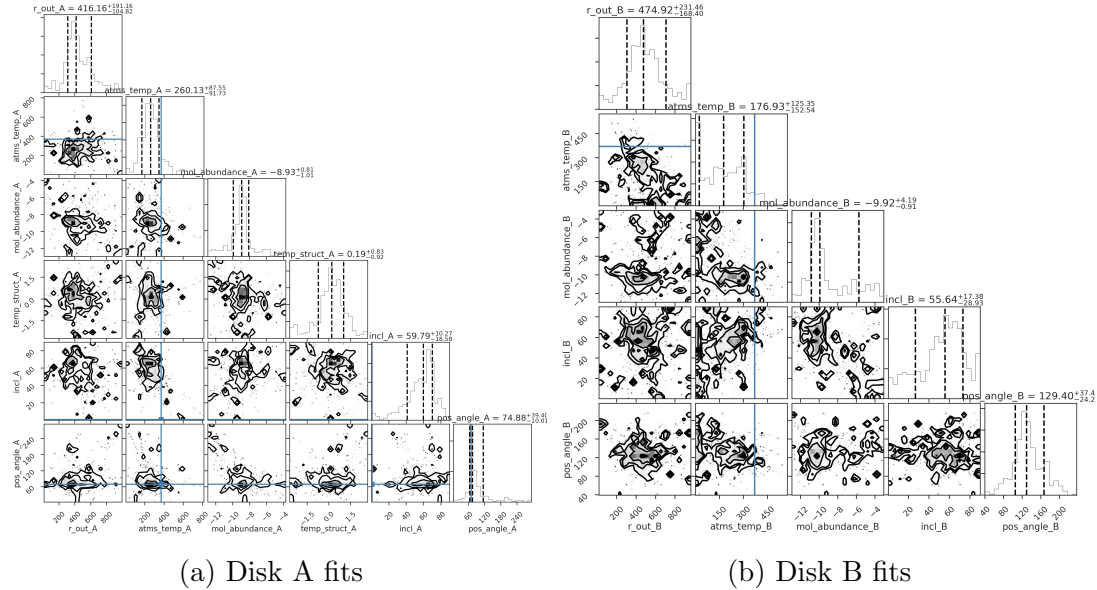


Figure 4.1: Since disk A and B's features are assumed to be independent, we may generate corner plots for each of their parameter spaces individually. Some analysis. REWORK: these are not the most recent ones

4.3 Fitting Procedure

Fitting of the data began with the analysis and partial removal of cloud contamination discussed in §3, resulting in the removal of baselines below a characteristic length for each line. With the data as clean as possible, position ($\Delta\alpha, \Delta\delta$) and velocity (v_{sys}) offsets were fit for. Offset fitting was executed only in the HCO⁺ line, thanks to the line's minimal contamination and high signal strength, and was performed as described in §4.2.1. With these values established, they were treated as fixed parameters for the remainder of the fitting process.

Table 4.2 presents a list of parameters, including $\Delta\alpha, \Delta\delta$, and v_{sys} , which were

left fixed throughout the MCMC runs. Since we are only modeling one line at a time, we are unable to constrain the vertical temperature structure and so fix T_{mid} and z_q . The selection of T_{mid} was made following Factor et al. (2017) to reflect the “CO snow line” shown by Qi et al. (2011)³, while the value of z_q was chosen, again following Factor et al. (2017), to be roughly double the disks’ scale heights, as shown in Rosenfeld et al. (2013). Since HCO^+ is optically thin, temperature and density are degenerate, so γ is set at 1 following Andrews et al. (2009), who showed this to be a reasonable value for disks in ρ Ophiuchus. Since our observations do not have enough spectral resolution to constrain the observations’ turbulent linewidth, we fix v_{turb} at around 1% of the sound speed, per Flaherty et al. (2015).

When fitting CO, we fix its abundance at the canonical value of 10^{-4} and instead fit for disk mass. Conversely, in our fits of HCO^+ and HCN emission, we fix M_{disk} at values drawn from Williams et al. (2014), which they infer from continuum flux measurements (and relying on the 100:1 gas/dust ratio discussed in §1). The remaining parameters are fit for using MCMC. We implement priors on each parameter, reported in Table 4.3. Gaussian priors are used for the fitting of both disks’ position angles, centered at values reported by Williams et al. (2014).

The results from the MCMC runs are presented below. To facilitate easier reading, accompanying figures are found at the end of the chapter.

4.3.1 $\text{HCO}^+(4-3)$ Fit

We began by fitting the HCO^+ line, using the MCMC methods explained above. Best fit and median values with 1σ uncertainties are given in Table 4.4, while corner plots, showing the posterior distributions of the individual line fit, is shown

³Although their measurements were made for sources in a different environment, the value gives us a reasonable starting point for our fits.

Table 4.2: Fixed Parameter Values

| Parameter | Description | Ref. | Fixed Value(s) | |
|---------------------------------------|--------------------------------|------|----------------|--------|
| | | | Disk A | Disk B |
| $\Delta\alpha$ ('') | RA offset from image center | 0 | 0.0002 | -1.006 |
| $\Delta\delta$ ('') | Dec offset from image center | 0 | 0.082 | -0.3 |
| v_{sys} (km s $^{-1}$) | Systemic velocity | 0 | 10.00 | 10.75 |
| i ($^{\circ}$) | Inclination | 1 | 65 | 45 |
| M_{\star} (M_{\odot}) | Stellar mass | 1 | 3.5 | 0.4 |
| Log M_{disk} (M_{\odot}) | Disk gas mass [*] | 1 | -1.11 | -1.55 |
| v_{turb} (km s $^{-1}$) | Turbulence velocity | 2 | | 0.081 |
| d (pc) | Distance | 3 | | 389 |
| R_c (au) | Critical radius | 1 | | 100 |
| γ | Radial density power law index | 4 | | 1 |
| z_q (au) | Disk scale height at 150 AU | 5 | | 29 |
| T_{mid} (K) | Midplane temp. at 150 AU | 6 | | 19 |

^{*} M_{disk} is fixed in our fitting of HCO $^{+}$ and HCN, and varied for CO.

⁰ Grid-search and/or elliptical fitting, as described in §4.2.1

¹ Williams et al. (2014)

² Flaherty et al. (2015)

³ Gaia Collaboration et al. (2018)

⁴ Andrews et al. (2009)

⁵ Factor et al. (2017)

⁶ Qi et al. (2011)

Table 4.3: Fit Parameter Values

| Parameter | Description | Prior |
|---------------------------------------|--|-------------|
| $\log X_{\text{mol}}$ | Molecular abundance, relative to H ₂ ^a | Log Uniform |
| q | Radial temperature power law index | Uniform |
| PA ($^{\circ}$) | Position Angle ^b | Gaussian |
| T_{atms} (K) | Atmospheric temperature at 150 AU | Uniform |
| Log M_{Disk} (M_{\odot}) | Disk gas mass [*] | Log Uniform |

^a For the CO line, X_{mol} is fixed at the literature value of 10^{-4} .

^b In our CO fit, disk B's position angle, PA, is fixed at the best-fit value from the HCO $^{+}$ fits.

^b For HCO $^{+}$ and HCN, disk mass was fixed at values from Williams et al. (2014).

in Fig. 4.2.

We see from the corner plots that, in general, the fits are quite well constrained. Uncertainties surrounding disk B's outer radius lead to some degeneracies, but overall this fit seems to be well managed. Inspection of the channel maps of the HCO⁺ data, best-fit model, and residuals (Fig. 4.3) show that, while the model seems to reproduce the data's morphological structure fairly well, fluxes are systematically low, leaving significant residuals.

Table 4.4: MCMC Fitting Results (HCO⁺)

| Parameter | Disk A | | Disk B | |
|------------------------------|---|----------|--|----------|
| | Median | Best Fit | Median | Best Fit |
| R _{out} (au) | 338.83 ⁺¹⁰ ₋₈ . | 342.22 | 268.17 ⁺⁸⁴ ₋₈₈ . | 155.48 |
| T _{atms} (K) | 221.99 ⁺¹⁰⁹ ₋₆₁ . | 209.48 | 182.09 ⁺⁶⁶ ₋₁₁₅ . | 284.81 |
| X _{HCO⁺} | -8.40 ^{+0.38} _{-0.24} | -8.36 | 10.32 ^{+0.32} _{-0.27} | -9.91 |
| PA (°) | 69.76 ^{+1.76} _{-1.24} | 70.17 | 131.86 ^{+10.97} _{-14.35} . | 120.25 |
| q | 0.73 ^{+0.32} _{-0.47} | 0.75 | [−0.5] | [−0.5] |
| lnprob | | | -28402 | |

* Values in [brackets] were fixed for this run.

4.3.2 HCN(4-3) Fit

Next we model HCN, using the same methods as for HCO⁺. As before, best fit and median values with 1σ uncertainties are given in Table 4.5, corner plots are shown in Fig. 4.5, and channel maps are presented in Fig. 4.6.

In the channel maps, we see that the fit is generally good, leaving fairly minimal residuals behind. The residuals do, however, highlight a stream of flux connecting the two disks, particularly at velocities around 9.4-10.2 km s⁻¹ that our model is unable to fit. This stream is most visible in the HCN line, compared to the

HCO⁺and CO maps.

For both disks, the posterior distribution of fits to outer radius is bimodal. This likely is a result of the MCMC walkers struggling to make sense of the above-mentioned bridge between the disks. This is particularly the case with disk B, where the walkers are distributed around 100 AU and around 350 AU. As a test, we can remove all steps in the MCMC chain where disk B's outer radius exceeds 220 AU (which is somewhere in the middle of the bimodality in the parameter's posterior distribution, but is still appreciably higher than the HCO⁺fit value of \sim 150 AU). Doing so brings HCO⁺and HCN into almost perfect agreement (<1%) on disk B's outer radius, while also increasing disk A's HCN abundance by more than an order of magnitude and pushing disk B's temperature up to more than twice the value found for the HCO⁺line. See Table ?? for a selection of the fit parameters, selected based on whether they change with the radius cut. As a visual check on whether this yields a better fit, Fig 4.4 shows HCN's first moment map with both best-fit disk B radii plotted.

Otherwise, the fit's posteriors are widely unimodal and less tightly constrained than those from the HCO⁺fits. There are no particularly noticeable degeneracies between parameters.

4.3.3 CO(3-2) Fit

Finally, we fit the CO(3-2) line. Despite the removal of baselines below $60\text{ k}\lambda$, the CO(3-2) line still shows significant cloud contamination in channels near the systemic velocity (Fig. 4.8). In an attempt to keep the MCMC walkers from trying to fit the contamination, we did not evaluate the χ^2 contribution of the channels with velocities between 9.88 and 12 km s^{-1} , which show the worst of

Table 4.5: MCMC Fitting Results (HCN)

| Parameter | Disk A | | Disk B | |
|-----------------------|--|----------|--|----------|
| | Median | Best Fit | Median | Best Fit |
| R _{out} (au) | 448.23 ^{+146.62} _{-120.17} | 334.68 | 217.02 ^{+133.53} _{-152.70} | 324.50 |
| T _{atms} (K) | 169.06 ^{+166.57} _{-95.87} | 140.95 | 155.78 ^{+188.93} _{-106.03} | 205.85 |
| X _{HCN} | -9.01 ^{+0.89} _{-0.55} | -7.62 | 10.81 ^{+0.95} _{-1.32} | -10.55 |
| PA (°) | 69.89 ^{+1.64} _{-1.81} | 69.30 | -134.77 ^{+16.15} _{-18.61} | 132.22 |
| q | 0.87 ^{+0.59} _{-0.59} | 0.72 | [-0.5] | [-0.5] |
| ln Likelihood | | | -30928.13 | |

* Values in [brackets] were fixed for this run.

Table 4.6: HCN Fits, R_{out, B} < 220

| | X _{mol} | R _{out} (au) | q | T _{atms} (K) |
|--------|------------------|-----------------------|--------|-----------------------|
| Disk A | -6.98 | 337.57 | 0.89 | 86.13 |
| Disk B | -10.3 | 145.57 | [-0.5] | 281.89 |

the clouds' effects. By choosing to not include these, we sacrifice some data, but the resulting fits are more representative of the structures we care about - the disks themselves - than they would be had we not sacrificed those channels. However, since it seems that this was insufficient, it is likely that it would have been preferable to exclude a far wider range of contaminated channels, likely from around 6.5 - 13.3 km s⁻¹.

Consequentially, the resulting fits are noticeably less certain than those of the HCO+ and HCN lines, featuring several jagged and bimodal posteriors, shown in Fig.4.7. Additionally, since the best-fit values disagree significantly with the results from the other lines (particularly in the T_{atms} for disk A, which is unrealistically low), we are unable to include these results in our analysis.

Despite this, the CO line seems to have had some marginal success in recovering

Table 4.7: MCMC Fitting Results (CO)

| Parameter | Disk A | | Disk B | |
|--|-------------------------------|----------|------------------------------|----------|
| | Median | Best Fit | Median | Best Fit |
| R_{out} (au) | $392.66^{+0.99.21}_{-114.75}$ | 492.76 | $199.45^{+83.34}_{-68.67}$ | 133.02 |
| T_{atms} (K) | $222.99^{+228.78}_{-218.54}$ | 2.87 | $273.39^{+132.27}_{-155.72}$ | 473.20 |
| $\log M_{\text{Disk}}$ (M_{\odot}) | $-2.56^{+2.03}_{-0.45}$ | -0.03 | $-4.76^{+0.36}_{-0.44}$ | -5.18 |
| PA (°) | $70.51^{+3.05}_{-2.71}$ | 72.28 | [136] | [136] |
| q | $-0.03^{+0.46}_{-0.47}$ | -0.03 | [-0.5] | [-0.5] |
| ln Likelihood | | | -33577.41 | |

* Values in [brackets] were fixed for this run.

disk radii, returning a best-fit value disk B that is within <10% of the HCO⁺line's reported value, and, although the best-fit radius for disk A is unreasonably high at nearly 500 AU, the model's 50th percentile fit is within 15% of the HCO⁺value. This seems to indicate that these data still have potential value if constrained appropriately.

Fig.5.2 show the resulting best-fit temperature and density structures in each line.

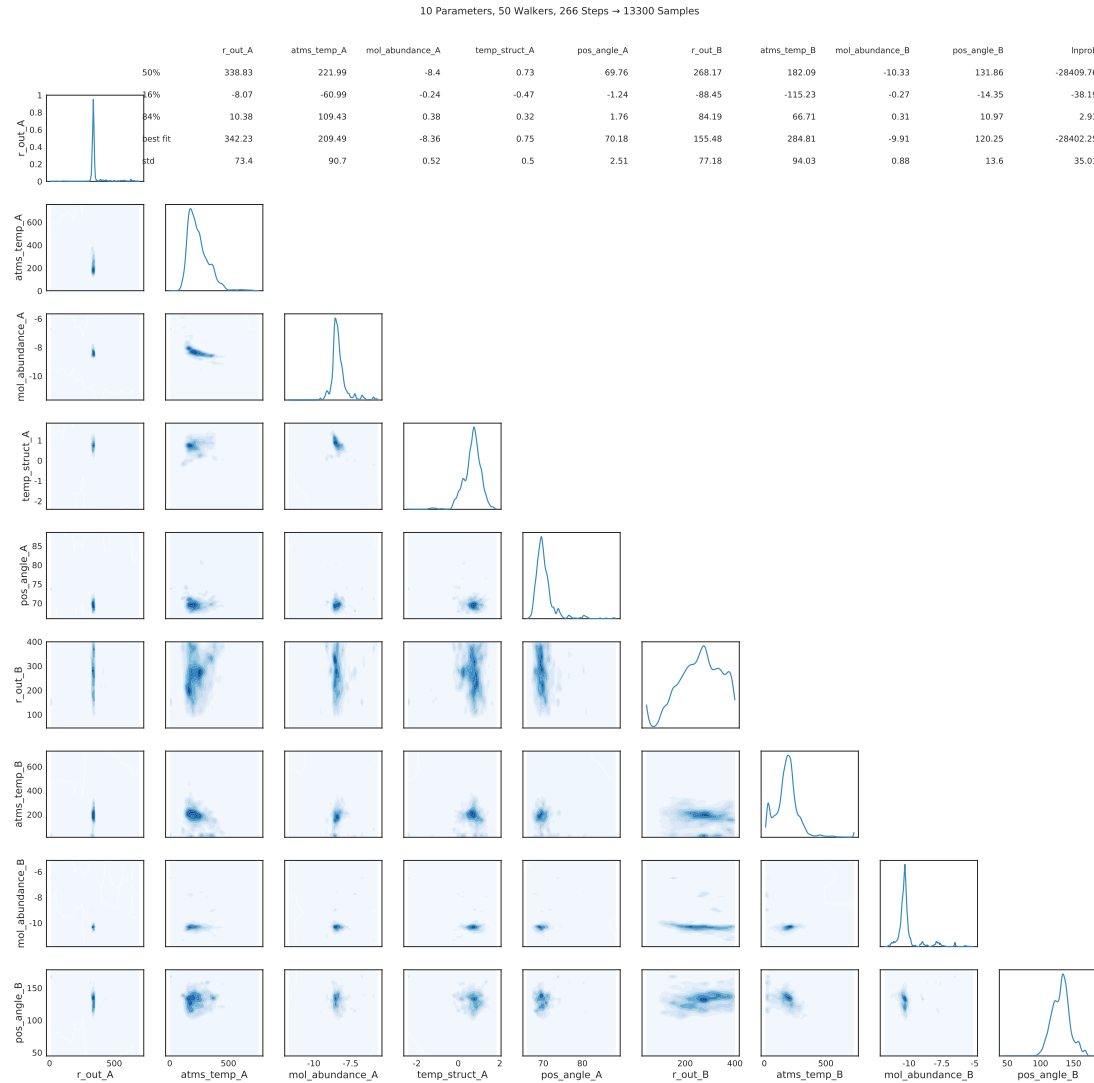


Figure 4.2: Cornerplots of results from MCMC fitting of HCO^+ emission.

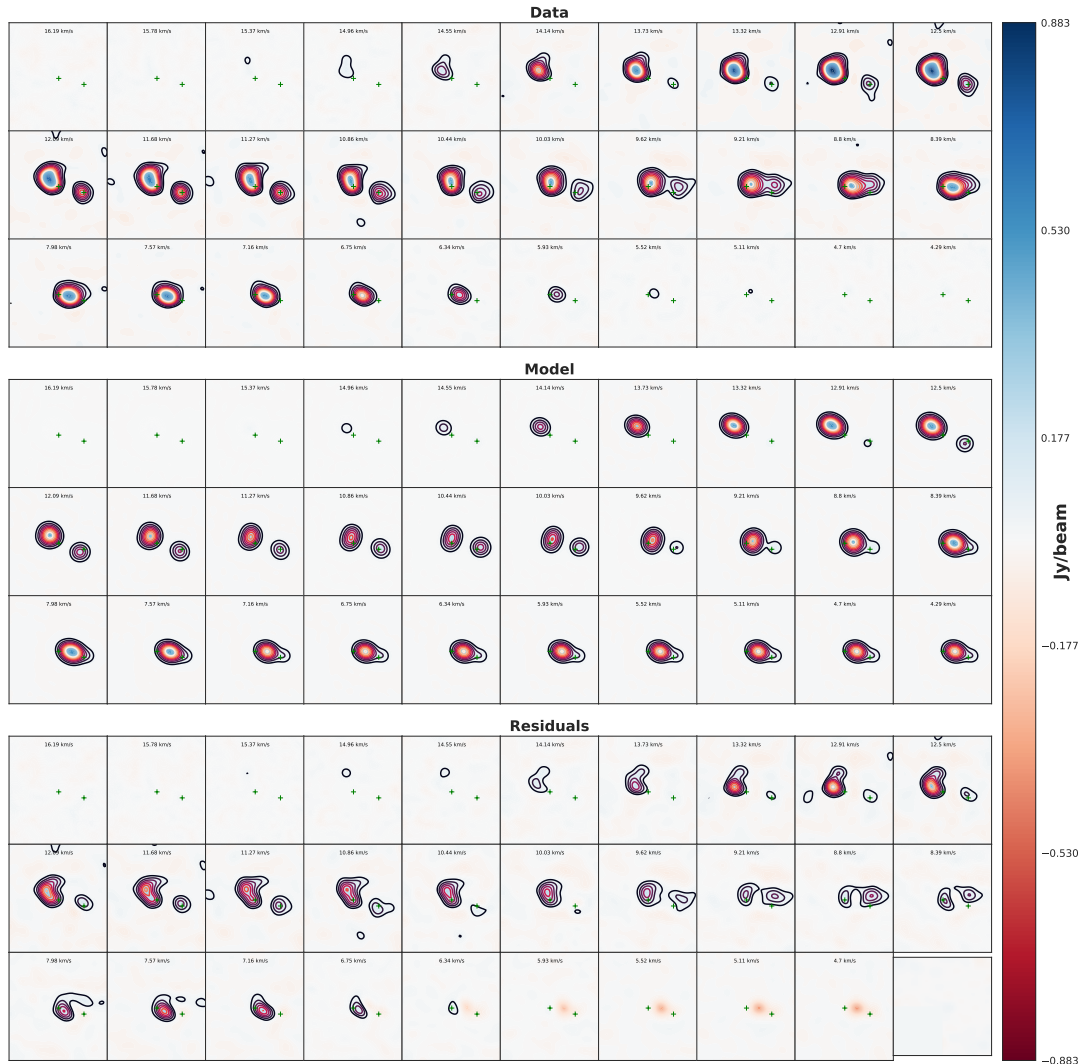


Figure 4.3: Channel maps of HCO⁺ emission data, as well as a best-fit model from MCMC fitting and residuals from the two.

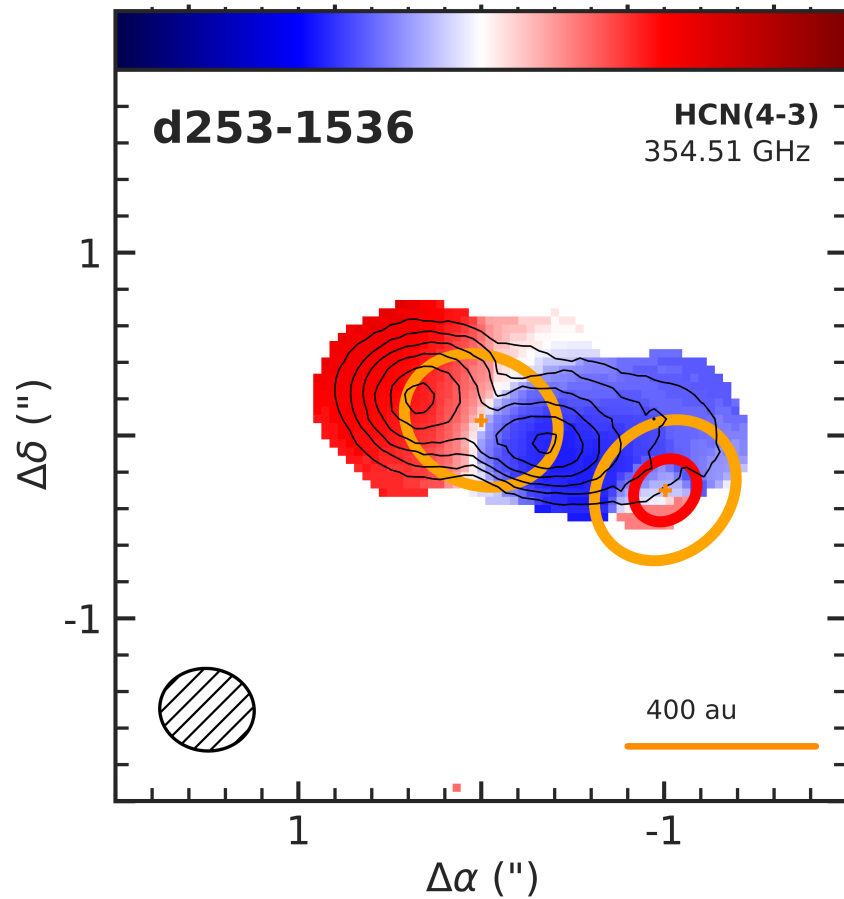


Figure 4.4: Moment-1 map of HCN emission, overlaid with ellipses described by each disk's best-fit position angle, inclination, and outer radius. For disk B, both the best-fit outer radius with and without the 220 AU a posteriori prior implemented (at 324 and 145 AU, respectively) are plotted.

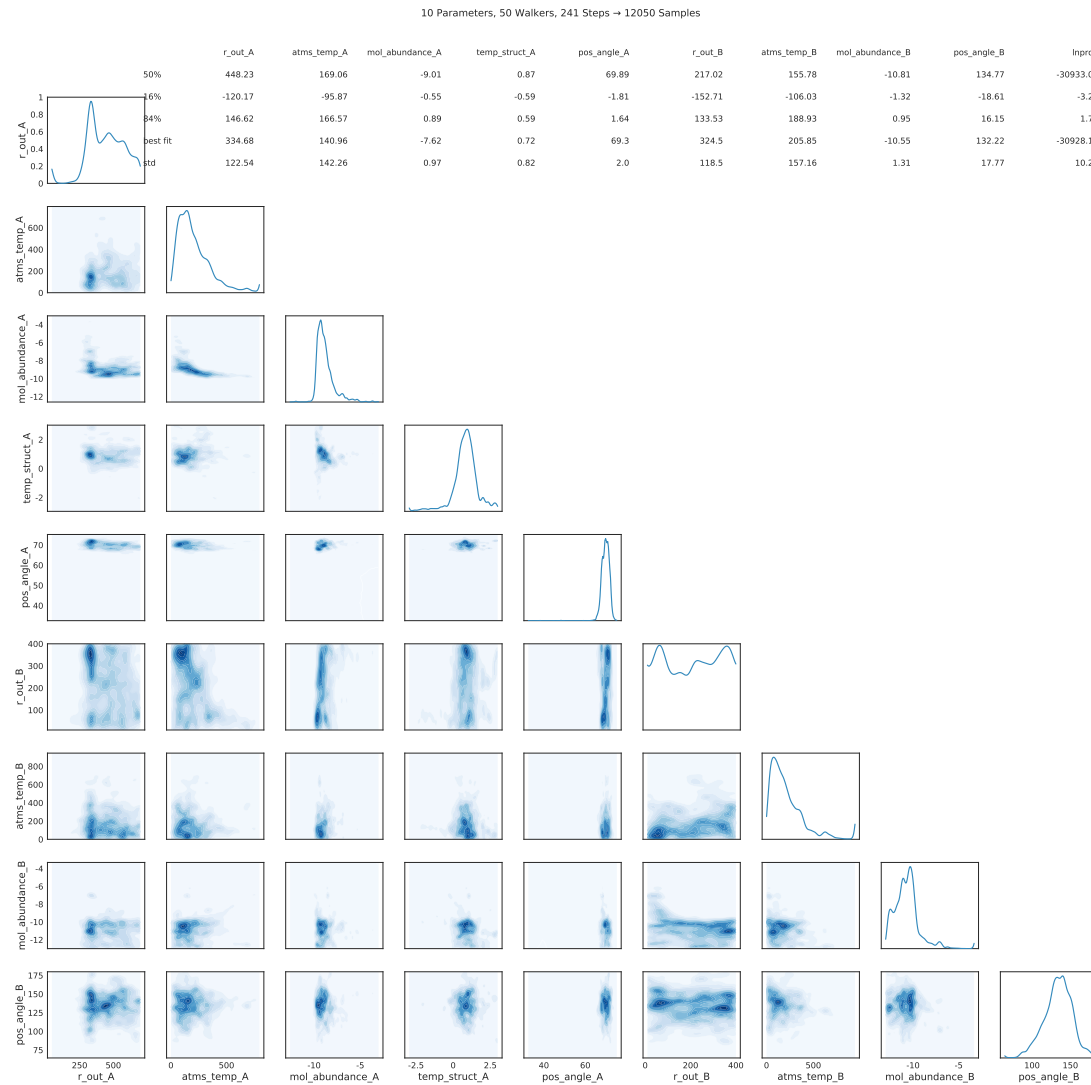


Figure 4.5: Cornerplots of results from MCMC fitting of HCN emission.

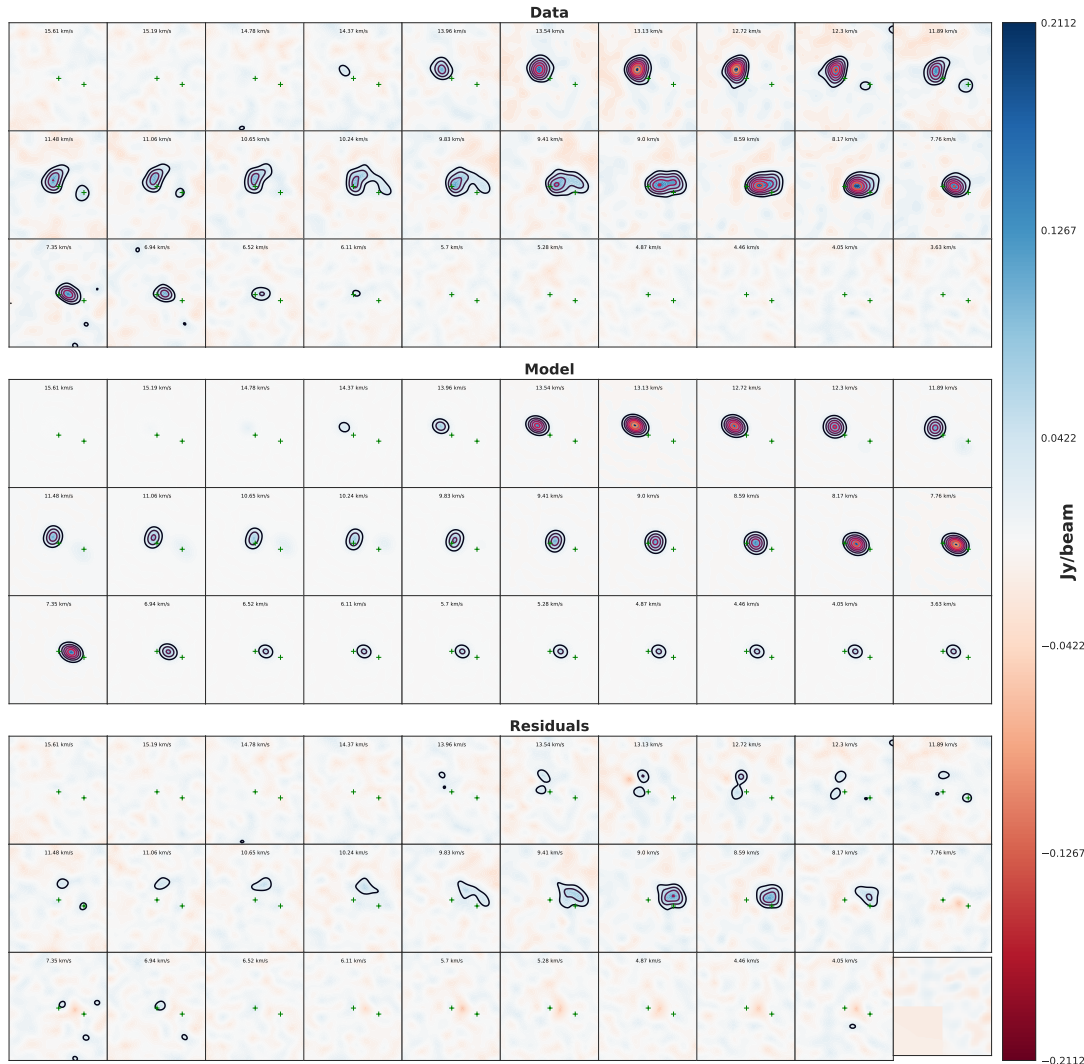


Figure 4.6: Channel maps of HCN emission data, as well as a best-fit model from MCMC fitting and residuals from the two.

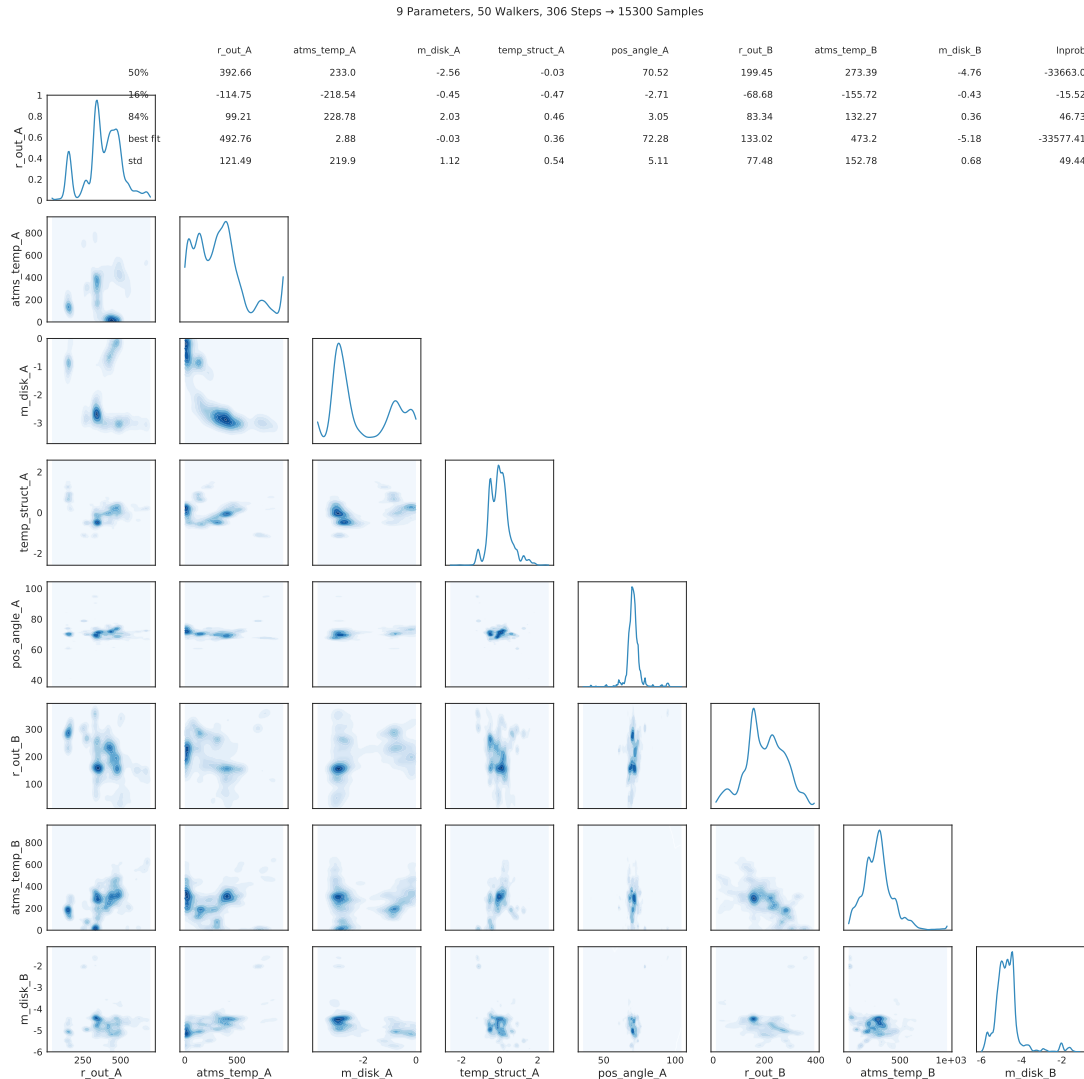


Figure 4.7: Cornerplots of results from MCMC fitting of HCN emission.

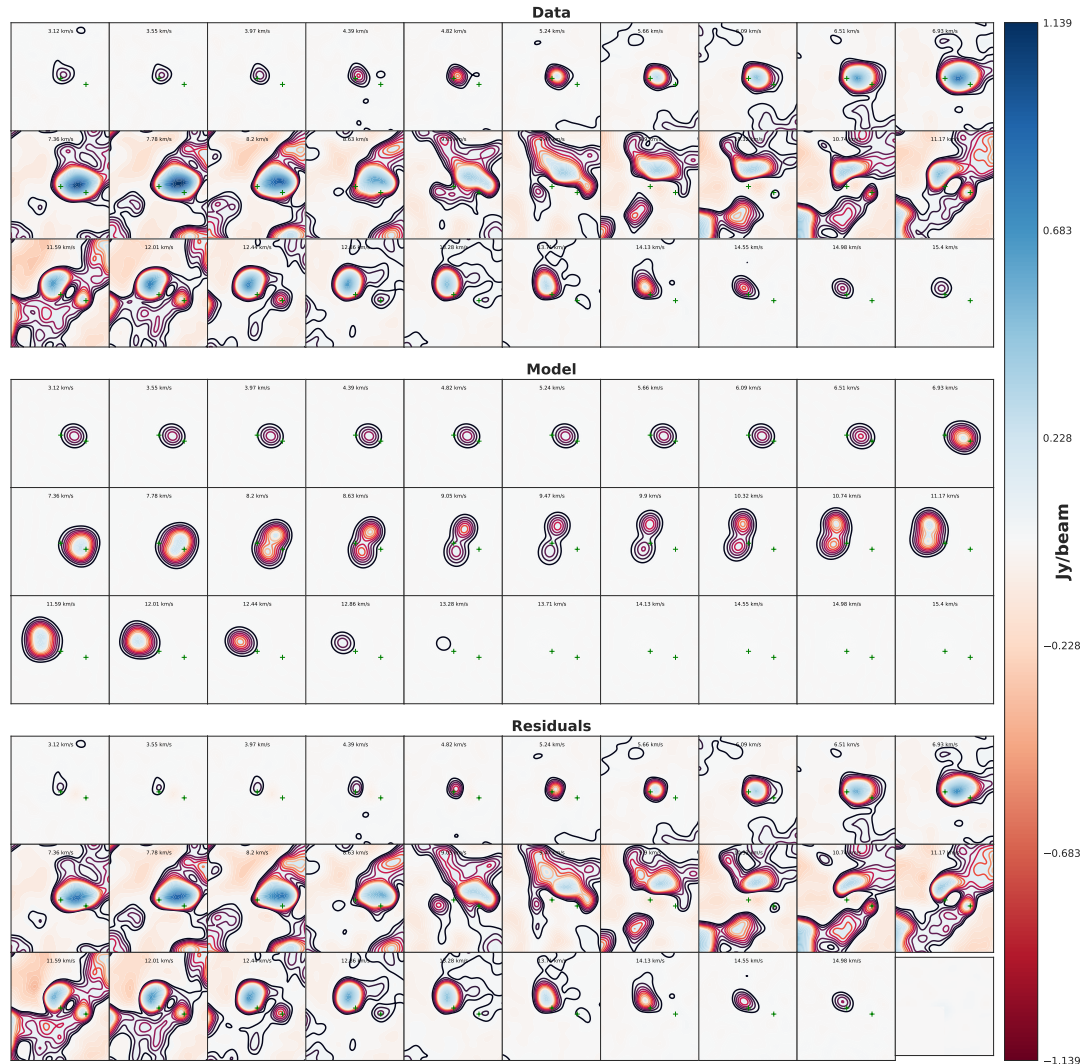


Figure 4.8: Channel maps of CO emission data, as well as a best-fit model from MCMC fitting and residuals from the two.

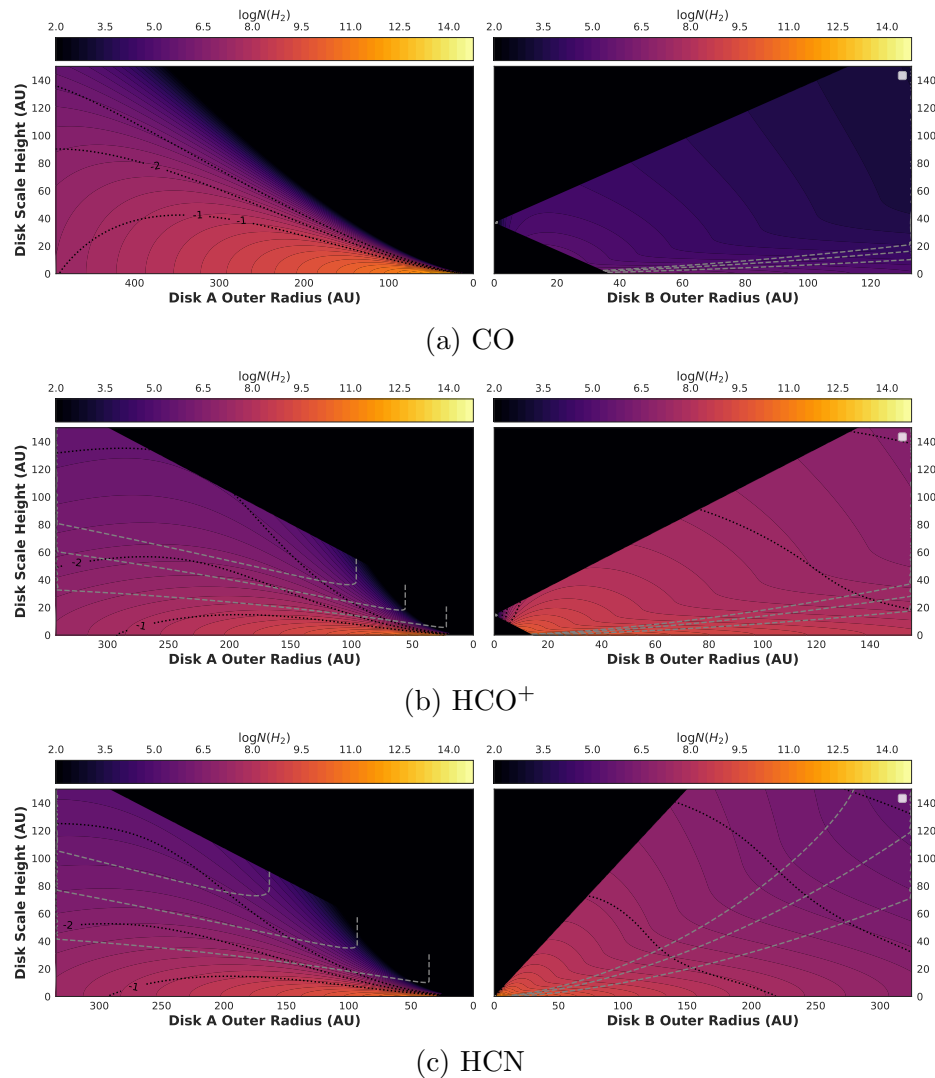


Figure 4.9: Density and temperature profiles for the best-fit models for CO, HCO^+ , and HCN.

Chapter 5

Discussion

With the disks now fit, we may interpret our results. Since this project was based around the question of how environment influences protoplanetary disks, we would like to compare our best fit values to other disks, including to one other from the ONC (Factor et al. 2017) as well as to others outside of it. We also consider how our results compare to modeling efforts.

5.1 Reflections on the Fits

Looking at the fits to our three molecular lines side by side, several things jump out. First and foremost, as discussed in §4.3.3, our attempts to fit the CO line were overwhelmed by the significant cloud contamination around the disk. If this run had converged, we would have used its disk mass results in the other runs, but since these results are not to be trusted, we instead continued to use the disks' mass values presented in Williams et al. (2014), which were inferred from continuum emission.

The HCO⁺ and HCN runs converged into impressive agreement, although their posteriors show that HCO⁺ line resulted in a much more confident model. Both lines show surprisingly high chemical abundances in disk A, while both also show significantly lower values for disk B abundances (discussed below). The two lines' fits for disk A's outer radius agree to within around 1% (although the HCN fit is

significantly less certain than the HCO⁺fit) and the lines' best-fit q values agree to within 15%. Atmospheric temperatures for disk A in both lines are large and significantly different, with the HCO⁺line preferring a temperature 50% greater than HCN's, but this is at least somewhat expected, as the two molecules are emitting from different regions of the disk and thus could reflect different regions of its temperature profile. In both lines, disk A's temperature structure power law index, q , is decidedly positive, although we expect this parameter to not settle with absolute certainty on a single value, since the observations don't have enough spatial resolution to constrain it tightly.

Fits for disk B are systematically less well constrained, since it is smaller, unresolved, and more easily overrun by excess emission from disk A and cloud contamination. Still, save for the disk's outer radius fit, all parameters are generally within the range of expected values.

As discussed in §4.3.2, a posteriori cuts of the HCN model's MCMC chain limiting disk B's outer radius to ≥ 220 AU changes the best-fit parameters significantly, most notably leading the fits of disk B's outer radius in HCO⁺and HCN into agreement and pushing disk A's HCN abundance more than a full order of magnitude higher, and into nearly perfect agreement with results from HCN fitting in Factor et al. (2017). Whether this is a reasonable thing to do is not clear to me.

We see in the HCN channel maps an area of significant flux coming from between disks around $v = 10.24 - 9.83$. This may be region where the two disks are interacting, a possibility that our model does not take into account. The feature is less clearly present in HCO⁺and invisible in CO, likely overrun by cloud contamination.

That each disk's abundances are so different from one another is something of

a surprise. Both disks have fairly similar ratios of the two emitting molecules: disk A's HCO^+/HCN ratio of log abundances is 1.09, while disk B's is 0.95¹. Williams et al. (2014) posit that wide binaries (systems with separations ≥ 300 au), such as this one, do not form in the same initial cloud structures². If this is the case, the notable differences in abundances between disk A and disk B could indicate that the disks in d253-1536 formed separately in clouds with different chemical compositions before joining together later. This is, of course, entirely speculative, but is a possibility.

5.2 Comparison with the Literature

We would now like to contextualize our results in the context of the larger field of protoplanetary disk studies.

5.2.1 Line Emission Modeling

In Table 5.1 we compare our results to those from other studies that have modeled line emission from protoplanetary disks. The most immediately relevant of these is the work by Factor et al. (2017), in which they use a similar modeling technique to characterize another ONC proplyd from the same survey as our binary, and thus represents the only other disk studied in this way that is also in a high-mass star forming region. The others are well-studied disks in low-mass regions. We may compare our temperature profiles and abundance to these other systems and look for variations from expected values.

Comparing our results for disk A to these other studies, we can see that our

¹These ratios become 1.21 for disk A and unity for disk B if the disk B radius cut is made.

²Jonathan doesn't actually put any references on this; I have no idea where he got it from. He just puts in references to other papers looking at misaligned binaries

Table 5.1: Disk Parameter List

| Reference | Source | Line | q | $\log X_{\text{mol}}$ | Atms. | Temp |
|--------------------------------------|------------|---|---------|-----------------------|-------|------|
| This study | d253-1536a | $\text{HCO}^+(4-3)$ | 0.66 | -7.96 | 151 | |
| | d253-1536a | $\text{HCN}(4-3)$ | 0.72 | -7.62 | 140 | |
| | d253-1536a | $\text{CO}(3-2)^a$ | 0.40 | [-4] | 1 | |
| Factor et al. (2017) | d216-0939 | $\text{HCO}^+(4-3)$ | 0.17 | -10.08 | 190 | |
| | d216-0939 | $\text{CO}(3-2)$ | -0.33 | [-4] | 70 | |
| | d216-0939 | $\text{HCN}(4-3)$ | -0.18 | -6.7 | 19 | |
| Flaherty et al. (2015) | HD163296 | $\text{CO}(3-2)$ | -0.22 | [-4] | 94 | |
| | HD163296 | $\text{CO}(2-1)$ | -0.27 | [-4] | 79 | |
| Hughes et al. (2008) ^b | A bunch | $\text{CO}(3-2)$ | - | [-4] | - | |
| Rosenfeld et al. (2012) ^b | V4046 Sgr | $^{12}\text{CO}(2-1)$ | -0.63 | [-4] | - | |
| Flaherty et al. (2017) ^c | HD163296 | $\text{DCO}^+(3-2)$ | [-2.22] | -10.79 | [94] | |
| Zhang et al. (2017) | TW Hya | $^{13}\text{C}^{18}\text{O}(3-2), \text{C}^{18}\text{O}(3-2)$ | -0.47 | -7.96 | 151 | |
| Flaherty et al. (2018) ^d | TW Hya | $\text{CO}(6-5, 3-2, 2-1)$ | -0.46 | [-4] | 31 | |

* Values in [brackets] were fixed during fitting.

atmospheric temperatures in $\text{HCO}^+(4-3)$ and $\text{HCN}(4-3)$ are consistent with the results of the HCO^+ fit in Factor et al. (2017). They are, however, significantly higher than any other study’s fit.

Additionally, our temperature structures for both HCO^+ and HCN are solidly positive, reflecting a temperature structure that increases with radius. As with the atmospheric temperature, this is contrasted by all other results, which have moderately negative values, save again for that of the Factor et al. (2017) HCO^+ line, which is also positive but less so than in our fits. Our positive values stand somewhat in contrast to the q value of $-0.5_{-0.1}^{0.2}$ predicted by Dartois et al. (2003) for a geometrically flat, optically thin disk.

Our molecular abundances for each disk vary from those reported in the Factor et al. (2017) paper, the only other study to model HCO^+ emission. In it, they re-

port finding canonical values for the HCO⁺line ($\log X_{HCO^+} = -10.04$) and unexpectedly high values for -6.7 , contrasted by our findings of -8.36 and -7.62 , respectively³.

We may also compare these abundances to theoretical modeling efforts. Walsh et al. (2010) developed radial and vertical chemical models for an imaginary isolated protoplanetary disk around a T-Tauri star (a system similar to the famous TW Hya), studying molecular abundance distributions throughout the disk for molecules within ALMA’s reach. They showed that log abundances in their models for HCO⁺varied from -8 to -12 , -7 to -12 for HCN, and -4 to -9 for CO. The authors then built on this model by adding robust modeling of externally-driven UV and X-ray ionization (Walsh et al. 2012) and applying it to the same disk system, this time with an O star nearby providing ionizing photons (Walsh et al. 2013). They then make the same molecular abundance distribution maps as before (see Fig. 5.1). The authors note that, in their model photoionized disk, HCO⁺column density increases by a factor of 6.3 relative to the isolated disk, whereas HCN and CO column densities remain constant through ionization⁴. They also note that the ionized disks have much higher gas temperatures, $\gg 50$ K, which is consistent with our findings.

Although our modeling assumes a constant chemical abundance across the whole disk, these models offer a way to confirm that our results are within the predicted ranges, despite the fact that the HCO⁺abundance is significantly higher than the values found by other studies.

³Although, as described above, removing samples with large outer radii for disk B pushes disk A’s HCN abundance to -6.98 , within the uncertainties of their HCN fit.

⁴This would be useful if we had an estimation of what the HCO⁺/HCN ratio would be in these two disks. They do have column density ratios in Walsh13; is it reasonable to say (I guess it would have to be in the case of optically thin emission) that col dens \propto abundance? If that were the case then we’d be golden.

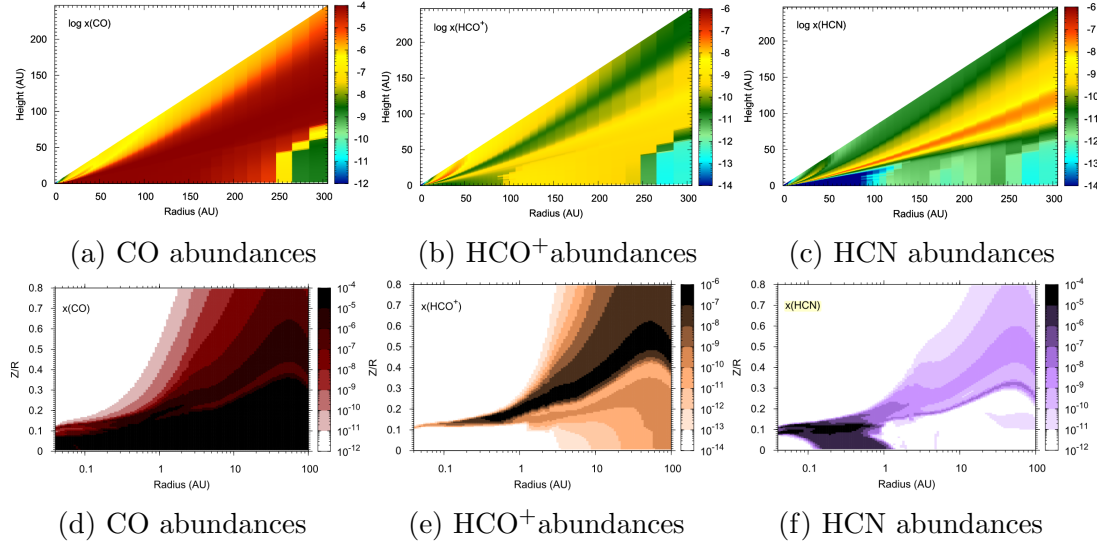


Figure 5.1: Models showing radial and vertical distributions of CO, HCO⁺, and HCN in a simulated disk around a T-Tauri star. The top row shows the profiles of isolated disks (Walsh et al. 2010), while the bottom row shows the profiles of disks being irradiated by a nearby O star (Walsh et al. 2013). Note that bottom row is on a log scale and only covers the inner 100 AU of the disk, while the top row is linearly scaled and shows a 300AU stretch. *It seems like only having one of these sets of images would make more sense.*

5.2.2 Population Comparison

We can also compare our disks' mass and radius to other protoplanetary disks. While these features may provide less nuanced insight, they are more easily measured, giving us a broader sample of disks to compare ours to. For these comparisons, we again draw on the disks' inferred gas mass measurements made by Williams et al. (2014), which carry with them significant uncertainty on account of the 100:1 assumed gas:dust ratio (as described in §1). As such, the values we use for the masses of disk A and disk B are $0.075 M_{\odot}$ and $0.029 M_{\odot}$ (78.66 and 29.88 Jovian masses), respectively. Our best-fit values for radii from the MCMC models were around 337 and 145 AU, respectively.

In the survey that originally provided these data, Mann et al. (2014) provided

initial disk masses, as well as semi-minor and -major axes of the disks, approximate measures of the disks' radial extents. Disk A in the present system was, by their measure, the most massive disk in the study, 75% more massive than the study's next most massive disk, d216-0939 (which was the subject of Factor et al. (2017)); disk B was the fifth most massive. Disk A had the study's fourth largest semi-major axis⁵. The authors did not fit disk B's radial extent; however, our measurement of 145 AU would make it the eleventh (out of 22) largest disk in the survey. Thus, disk A is on the very high end of the study's mass and radius range, while disk B is apparently quite dense and of median radial extent.

In ?, the authors analyze several CO isotopologues to retrieve the gas masses of 34 protoplanetary disks in Lupus. In it, they report surprisingly low masses, reflective of their calculated gas/dust ratios, which systematically fall well below the traditional value of 100. Their resulting gas masses are far smaller than those found by Mann et al. (2014) in the ONC; here, most of the survey's masses are between 10^{-5} to $10^{-3} M_{\odot}$, with the most massive at $1.5 \times 10^{-3} M_{\odot}$ (1.6 Jovian masses). since the disks were not spatially resolved, radii were not measured.

Ansdell et al. (2016) and Ansdell et al. (2018) characterized the mass (both dust and gas) and radius distributions of protoplanetary disks in Lupus using CO isotopologues and continuum emission. To derive gas masses, they assumed a CO/H₂ ratio of 10^{-4} and then used the isotopologues' ratios to find total masses. Of these gas masses that they were able to constrain, they found disks to range from around 1-10 Jovian masses.

Eisner et al. (2018) conducted a particularly comprehensive survey of disks in σ Ori, a young cluster in the ONC, north of M42 and M43. In their survey, they

⁵The authors' measurement of disk A's semi-major axis, at 268 au, is 20% smaller than our fit measurements. The survey's reported semi-major axis for d216-0939 was also smaller than the fit value in Factor et al. (2017), though by only 6%.

trace dust masses, so maybe it's not terribly useful. Still, they note that disks in their survey are particularly compact.

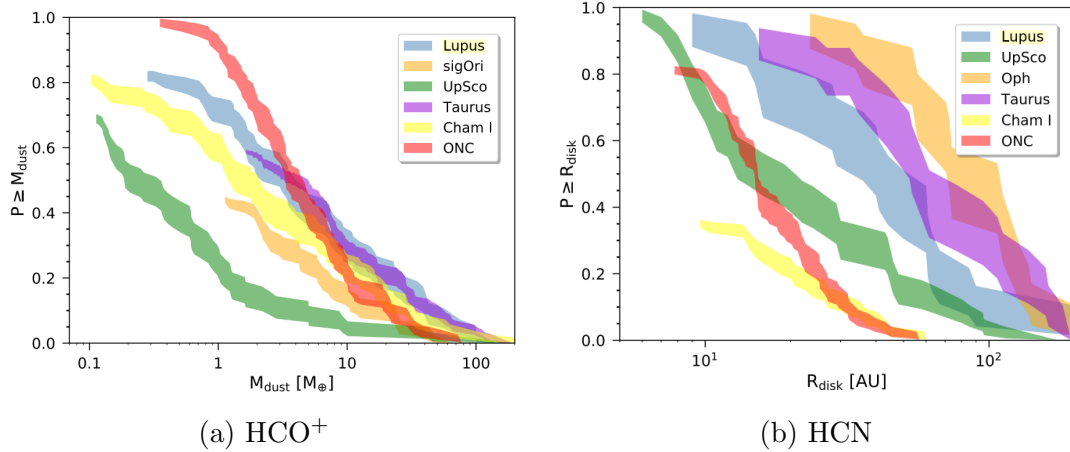


Figure 5.2: Some stuff from Eisner2018.

I don't really know what else to say here. Seems like ours are big, dense disks. Would be really nice to calculate that gas mass on my own.

5.3 Remarks

These disks appear to be somewhat atypically large and dense. They may have formed separately. More work should be done. Etc

This section still feels a little incomplete; I don't really know what else to do with it. Would love to hear your thoughts/guidance.

Chapter 6

Summary

We have presented ALMA observations tracing line emission CO(3-2), HCO⁺(4-3), HCN(4-3), and CS(7-6) of d253-1536, a binary of young protoplanetary disks in the M43 region of the Orion Nebula Cluster. We model the HCO⁺, HCN, and CO emission using a gas model that assumes Keplerian rotation, local thermodynamic equilibrium, and hydrostatic equilibrium to develop synthetic images of a model disk. We then use an affine-invariant Markov Chain Monte Carlo (MCMC) algorithm to explore parameter space and identify regions of best fit, comparing each model image to our data using a χ^2 test. By fitting each line's emission, we are able to statistically characterize elements of the disks' chemical compositions and their temperature structures.

We find atmospheric temperatures that are somewhat atypically high relative to studies of other protoplanetary disks. Additionally, we find that in disk A, the binary's eastern disk, HCO⁺ and HCN abundances are two orders of magnitude higher than in disk B, possibly indicating that the disks formed separately, as suggested by Williams et al. (2014), before joining into their current loose binary. While these values are deviations from most of the literature, they do align with the results of work done by Factor et al. (2017) in fitting HCO⁺ emission from another disk in the same survey as these, using similar methods of analysis.

With temperature, density, and chemical characterizations of these disks, we

may finally begin to answer the question of how unique we - the Solar System - are. Probably more justification here.

Thanks to Meredith, Kevin, Sam, others?

J.P. is funded by the Connecticut Space Grant's Undergraduate Research Fellowship, Undergraduate Scholarship, and Travel Grant, as well as Wesleyan University's Research in the Sciences Fellowship.

This paper makes use of the following ALMA data: ADS/JAO.ALMA#2011.0.00028.S.

ALMA is a partnership of ESO (representing its member states), NSF (USA) and NINS (Japan), together with NRC (Canada), MOST and ASIAA (Taiwan), and KASI (Republic of Korea), in cooperation with the Republic of Chile. The Joint ALMA Observatory is operated by ESO, AUI/NRAO and NAOJ. The National Radio Astronomy Observatory is a facility of the National Science Foundation operated under cooperative agreement by Associated Universities, Inc.

This project made heavy use of the following open-source analysis tools: Pandas (McKinney 2010, 2011), NumPy (Van Der Walt et al. 2011), emcee (Foreman-mackey et al. 2013)

Bibliography

- ^{a b c}Aikawa, Y., & Herbst, E. 2003, *Astron. Astrophys.*, 371, 1107
- Anderson, K. R., Adams, F. C., & Calvet, N. 2013, *Astrophys. J.*, 774
- Andrews, S. M., et al. 2018, *Astrophys. J. Lett.*
- Andrews, S. M., & Williams, J. P. 2005, *Astrophys. J.*, 631, 1134
- . 2007, *Astrophys. J.*, 1
- Andrews, S. M., Wilner, D. J., Hughes, A. M., Qi, C., & Dullemond, C. P. 2009, *Astrophys. J.*, 700, 1502
- Ansdell, M., Williams, J. P., Manara, C. F., Miotello, A., Facchini, S., van der Marel, N., Testi, L., & van Dishoeck, E. F. 2017, *Astron. J.*, 153, 240
- Ansdell, M., et al. 2018
- . 2016, ALMA Survey of Lupus Protoplanetary Disks I: Dust and Gas Masses No. May
- Bontemps, S., et al. 2001, *Astron. Astrophys.*
- Bosman, A. D., van Dishoeck, E. F., & Walsh, C. 2018, *Astron. Astrophys.*
- Butler, B. 2012, ALMA Memo 594
- Chiang, E., & Laughlin, G. 2013, *Mon. Not. R. Astron. Soc.*, 431, 3444
- Cieza, L. A., et al. 2019, *Mon. Not. R. Astron. Soc.*, 482, 698
- Cleeves, L. I., Bergin, E. A., & Adams, F. C. 2014, *Astrophys. J.*, 794

- Cleeves, L. I., Bergin, E. A., Bethell, T. J., Calvet, N., Fogel, J. K. J., Sauter, J., & Wolf, S. 2011, *Astrophys. J. Lett.*, 743, 1
- Cleeves, L. I., Bergin, E. A., Qi, C., Adams, F. C., & Öberg, K. I. 2015, *Astrophys. J.*, 799
- Collaboration, T. E. H. T. 2019, *Astrophys. J.*, 1
- Combes, F., et al. 2018, *Astron. Astrophys.*, 79, 1
- Dartois, E., Dutrey, A., & Guilloteau, S. 2003, *Astron. Astrophys.*, 399, 773
- de Gregorio-Monsalvo, I., et al. 2013, *Astron. Astrophys.*, 557, A133
- Duchêne, G., & Kraus, A. 2013, *Annu. Rev. Astron. Astrophys.*, 1
- Dullemond, C. P., & Monnier, J. D. 2010, *Annu. Rev. Astron. Astrophys.*, 1
- Eisner, J. A., et al. 2018, *Astrophys. J.*
- Eistrup, C., Walsh, C., & van Dishoeck, E. F. 2017, *Astron. Astrophys.*
- F. Shu, F. Adams, S. L. 1987, *Annu. Rev. Astron. Astrophys.*
- Factor, S. M., et al. 2017, *Astrophys. J.*
- Flaherty, K. M., et al. 2017, 163296, 1
- Flaherty, K. M., Hughes, A. M., Rosenfeld, K. A., Andrews, S. M., Chiang, E., Simon, J. B., Kerzner, S., & Wilner, D. J. 2015, *Astrophys. J.*, 813, 1
- Flaherty, K. M., Hughes, A. M., Teague, R., Simon, J. B., Andrews, S. M., & Wilner, D. J. 2018, 1

- Fogel, J. K., Bethell, T. J., Bergin, E. A., Calvet, N., & Semenov, D. 2011, *Astrophys. J.*, 726
- Foreman-mackey, D., Hogg, D. W., Lang, D., & Goodman, J. 2013, *Publ. Astron. Soc. Pacific*
- Gaia Collaboration. 2016, *Astron. Astrophys.*
- Gaia Collaboration, Brown, A. G. A., Vallenari, A., Prusti, T., de Bruijne, J. H. J., Babusiaux, C., & Bailer-Jones, C. A. L. 2018, *Astron. Astrophys.*
- Gaidos, E., Krot, A. N., Williams, J. P., & Raymond, S. N. 2009, *Astrophys. J.*, 696, 1854
- Goodman, J., & Weare, J. 2010, *Math. Sci. Publ.*, 5, 1
- Hartmann, L., Calvet, N., Gullbring, E., & D'Alessio, P. 1998, *Astrophys. J.*, 741
- Haworth, T. J., Boubert, D., Facchini, S., Bisbas, T. G., & Clarke, C. J. 2016, *Mon. Not. R. Astron. Soc.*, 463, 3616
- Henney, W. J., & O'Dell, C. R. 1999, *Astron. J.*, 118, 2350
- Herrera-Martín, A., Hendry, M., Gonzalez-Morales, A. X., & Ureña-López, L. A. 2019, *Astrophys. J.*, 872, 11
- Hildebrand, R. 1983, *Q. J. R. Astron. Soc.*, 24, 267
- Hogbom, J. 1974, *Astron. Astrophys. Suppl.*
- Hubickyj, O., Bodenheimer, P., & Lissauer, J. J. 2005, *Icarus*, 179, 415
- Hughes, A. M. 2010, PhD thesis, Harvard University

- Hughes, A. M., Duchene, G., & Matthews, B. 2018, Annu. Rev. Astron. Astrophys., 1
- Hughes, A. M., et al. 2017, *Astrophys. J.*, 839, 86
- Hughes, A. M., Wilner, D. J., Qi, C., & Hogerheijde, M. R. 2008, *Astrophys. J.*
- Jensen, E. L., & Akeson, R. 2014, *Nature*, 511, 567
- Johnstone, D., Hollenbach, D., & Bally, J. 1998, *Astrophys. J.*, 499, 758
- Kalyaan, A., Desch, S. J., & Monga, N. 2015, *Astrophys. J.*, 815, 112
- Kenyon, S. J., Gomez, M., & Whitney, B. A. 2008, *Handb. Star Form. Reg.* Vol. I, I
- Kruijssen, J. M. D., & Longmore, S. N. 2019, 1
- Kuchner, M. J. 2004, *Astrophys. J.*, 612, 1147
- Lada, C. J., & Lada, E. A. 2003, Annu. Rev. Astron. Astrophys., 57
- Liu, Y., et al. 2018, 75, 1
- Luhman, K. L., Allen, P. R., Espaillat, C., Hartmann, L., & Calvet, N. 2010, *Astrophys. Journal, Suppl. Ser.*, 186, 111
- Lynden-Bell, D., & Pringle, J. E. 1974, *Mon. Not. R. Astron. Soc.*, 168, 603
- Mann, R. K., Andrews, S. M., Eisner, J. A., Williams, J. P., Meyer, M. R., Di Francesco, J., Carpenter, J. M., & Johnstone, D. 2015, *Astrophys. J.*, 802, 1
- Mann, R. K., et al. 2014, *Astrophys. J.*, 784, 1
- Mann, R. K., & Williams, J. P. 2009, *Astrophys. J.*, 699, 1994

- McKee, C. F., & Ostriker, E. C. 2007, Annu. Rev. Astron. Astrophys., 565
- McKinney, W. 2010, Proc. 9th Python Sci. Conf., 1697900, 50
- . 2011, 19, 583
- McMullin, J. P., Waters, B., Schiebel, D., Young, W., & Golap, K. 2007, Astron. Soc. Pacific Conf. Ser., 376, 127
- Miotello, A. 2017, Proc. Int. Astron. Union, 13, 124
- Observatory, A. ????, Origins — ALMA
- Ovelar, M. d. J., Kruijssen, J. M. D., Bressert, E., Testi, L., Bastian, N., & Cabrera, H. C. 2012, 1, 1
- Pavlyuchenkov, Y., Semenov, D., Henning, T., Guilloteau, S., Pietu, V., Launhardt, R., & Dutrey, A. 2007, *Astrophys. J.*, 669, 1262
- Podio, L., et al. 2019, *Astron. Astrophys.*, 6, 1
- Qi, C., D'Alessio, P., Berg, K. I., Wilner, D. J., Hughes, A. M., Andrews, S. M., & Ayala, S. 2011, *Astrophys. J.*, 740
- Raymond, S. N., & Cossou, C. 2014, *Mon. Not. R. Astron. Soc. Lett.*, 440
- Reboussin, L., Wakelam, V., Guilloteau, S., Hersant, F., & Dutrey, A. 2015, *Astron. Astrophys.*, 579, A82
- Reggiani, M., Robberto, M., Da Rio, N., Meyer, M. R., Soderblom, D. R., & Ricci, L. 2011, *Astron. Astrophys.*, 534, A83
- Ricci, L., Robberto, M., & Soderblom, D. R. 2008, *Astron. J.*, 136, 2136

- Ricci, L., Testi, L., Williams, J. P., Mann, R. K., & Birnstiel, T. 2011, *Astrophys. J. Lett.*, 739, 1
- Robberto, M., et al. 2013, *Astrophys. Journal, Suppl. Ser.*, 207
- Rosenfeld, K. A., Andrews, S. M., Hughes, A. M., Wilner, D. J., & Qi, C. 2013, *Astrophys. J.*, 774
- Rosenfeld, K. A., Andrews, S. M., Wilner, D. J., & Stempels, H. 2012, *Astrophys. J.*, 806
- Salyk, C., Pontoppidan, K., Corder, S., Muñoz, D., Zhang, K., & Blake, G. A. 2014, *Astrophys. J.*, 792
- Sault, R. J., Teuben, P. J., & Wright, M. C. H. 1995, *Astron. Data Anal. Softw. Syst.*
- Schöier, F. L., van der Tak, F. F. S., van Dishoeck, E. F., & Black, J. H. 2005, *Astron. Astrophys.*, 432, 369
- Schwarz, K. R., Bergin, E. A., Cleeves, L. I., Blake, G. A., Zhang, K., Öberg, K. I., van Dishoeck, E. F., & Qi, C. 2016, *Astrophys. J.*, 0, 1
- Skilling, J., & Bryan, R. K. 1984, *Mon. Not. R. Astron. Soc.*, 211, 111
- Smith, N., Bally, J., Licht, D., & Walawender, J. 2005, *Astron. J.*, 129, 382
- Tachibana, S., Huss, G. R., Kita, N. T., Shimoda, G., & Morishita, Y. 2006, *Astrophys. J.*, 639, L87
- Tsiganis, K., Gomes, R., Morbidelli, A., & Levison, H. F. 2005, *Nature*, 435, 459

- Van Der Walt, S., Colbert, S. C., & Varoquaux, G. 2011, Comput. Sci. Eng., 13, 22
- van Dishoeck, E. F., & Blake, G. A. 1998, Astron. Astrophys.
- Vicente, S. M., & Alves, J. 2005, in Astron. Astrophys., Vol. 205, 214–216
- Walsh, C., et al. 2016, Astrophys. J., 823, L10
- Walsh, C., Millar, T. J., & Nomura, H. 2010, Astrophys. J., 722, 1607
- . 2013, Astrophys. J. Lett., 766, 1
- Walsh, C., Nomura, H., Millar, T. J., & Aikawa, Y. 2012, Astrophys. J., 747
- Walsh, K. J., Morbidelli, A., Raymond, S. N., O'Brien, D. P., & Mandell, A. M. 2011, Nature, 475, 206
- Weidenschilling, S. 1977, Astrophys. Space Sci.
- Wernecke, S. J., & D'Addario, L. R. 1977, IEEE Trans. Signal Process., 39, 1478
- Williams, J. P., & Best, W. M. J. 2014, Astrophys. J., 788
- Williams, J. P., & Cieza, L. A. 2011, Astrophys. J.
- Williams, J. P., et al. 2014, Annu. Rev. Astron. Astrophys., 796
- Xiao, L., & Chang, Q. 2018, Astrophys. J., 853, 22
- Yu, M., Evans, N. J., Dodson-Robinson, S. E., Willacy, K., & Turner, N. J. 2017, Astrophys. J., 1
- Zhang, K., Bergin, E. A., Blake, G. A., Cleeves, L. I., & Schwarz, K. R. 2017, Nat. Astron., 1